MOX-Report No. 61/2018

A Computational Framework for Fluid-Porous Structure Interaction with Large Structural Deformation

Zakerzadeh, R.; Zunino P.

MOX, Dipartimento di Matematica
Politecnico di Milano, Via Bonardi 9 - 20133 Milano (Italy)

mox-dmat@polimi.it http://mox.polimi.it

Title Page

Title:

A Computational Framework for Fluid-Porous Structure Interaction with Large Structural Deformation

Authors:

Rana Zakerzadeh[1], Paolo Zunino[2]

Author Affiliations:

[1] Center for Cardiovascular Simulation, Institute for Computational Engineering and Sciences (ICES), The University of Texas at Austin, Austin, TX, 78712, USA

[2] Modeling and Scientific Computing (MOX), Department of Mathematics, Politecnico di Milano, Milano, Italy

Corresponding Author:

Paolo Zunino, Ph.D.

Professor in Numerical Analysis

MOX, Dipartimento di Matematica

Politecnico di Milano

E-mail: paolo.zunino@polimi.it

Abstract: we study the effect of poroelasticity on fluid-structure interaction. More precisely, we analyze the role of fluid flow through a deformable porous matrix in the energy dissipation behavior of a poroelastic structure. For this purpose, we develop and use a nonlinear poroelastic computational model and apply it to the fluid-structure interaction simulations. We discretize the problem by means of the finite element method for the spatial approximation and using finite differences in time. The numerical discretization leads to a system of non-linear equations that are solved by Newton's method. We adopt a moving mesh algorithm, based on the Arbitrary Lagrangian Eulerian (ALE) method to handle large deformations of the structure. To reduce the computational cost, the coupled problem of free fluid, porous media flow and solid mechanics is split among its components and solved using a partitioned approach. Numerical results show that the flow through the porous matrix is responsible for generating a hysteresis loop in the stress versus displacement diagrams of the poroelastic structure. The sensitivity of this effect with respect to the parameters of the problem is also analyzed.

Keywords: Fluid-structure interaction; Poroelasticity; Finite deformations; Energy dissipation

1 Introduction

We consider the problem of the interaction between a free flow with a deformable poroelastic medium. Such a problem is of a great importance in a wide range of applications. The filtration of fluids through the porous media occurs in industrial processes involving air or oil filters, in cross-flow filtration procedures, and in geophysical applications such as modeling the groundwater flow in the deformable porous media. Another application of this problem is in the area of biology. Since most of soft tissues are fully saturated with water, poroelastic models are suitable to describe their deformations. Porous media equations have been used for modeling the blood flow in the myocardium [1, 2], to study drug and lipid transport in blood vessels [3-6], as well as the interstitial fluid in articular cartilage [7] and intervertebral discs [8]. Poroelasticity has also been applied to analyze the mechanical properties of the brain [9, 10]. The behavior of the poroelastic materials has been studied extensively, however only a few studies have included poroelastic models in Fluid-Structure Interaction (FSI) simulations, see for example [5, 11] and references therein. Since analytical results on existence of the solution for FSI problems can be found only for certain simplified systems, computational models play a significant role in this area. In the context of hemodynamics, considering arterial wall as an elastic structure is a common assumption in FSI simulations [12-14]. However, there are evidences that the arterial wall, like other soft tissues, shows a poroelastic behavior [15, 16]. For this reason, we adopt a Fluid- Porous Structure Interaction (FPSI) formulation.

Many studies in the context of FSI for arteries have the limitation of assuming small deformations to describe the arterial wall motion, such as [3, 5] and our previous study [17] where the interaction between a viscous fluid and a thick poroelastic structure with small displacement has been analyzed. In [1], finite elasticity has been adopted to give a description of

the mechanical behavior of the porous medium to model blood perfusion in the cardiac tissue. However, the authors simplify the problem by neglecting the blood flow equations and by considering a single poroviscoelastic compartment to model the tissue. Taylor et al. in [4] used a similar approach to study drug transport in the arterial wall using a porohyperelastic model. The advection-diffusion equation is solved for modeling mass transport in the tissue, while due to the complexity of the problem, the fluid flow within the arterial channel is neglected. More recent studies of the flow through hyperelastic, saturated porous media under finite deformations using the finite element method, have been proposed in [18, 19]. In particular, in [18] authors considered a general nonlinear poromechanical model and established a discrete energy estimation for the two-phase poromechanics formulation developed previously in [20]. Although the formulation in [18, 20] thoroughly covers the coupling between large deformations of the solid matrix and internal fluid flow of the porous medium (referred to as fluid-structure interaction in the aforementioned paper), but the interaction between the poroelastic media with an external fluid flow, namely fluid-porous structure interaction has not been explored.

Many of the previous studies on the FSI problems with large deformations have used the monolithic scheme for solving the FSI system in the nonlinear case, with various types of preconditioners [21, 22]. In [21] finite elasticity is applied to study the interaction between the blood flow and elastic arterial wall. In [6] porohyperelastic fluid-structure interaction is adopted using a monolithic approach. Furthermore, the interaction between the blood flow and porohyperelastic arterial model is coupled with mass transport analysis of lipids in the arterial wall. The design of partitioned algorithms for uncoupling the solution of the three sub-problems in the interaction between pulsatile flow and poroelastic material is still partially unexplored. In our previous works [23, 24] a loosely coupled scheme has been successfully developed and tested on 2D and 3D FPSI simulations. However, these studies were focused on the small deformation regime for the poroelastic structure. In this work our objective is to develop a computational model for nonlinear poroelastic structure coupled with fluid flow for the purpose of analyzing the influence of the model parameters on the energy dissipation in different loading regimes. A difficulty of using finite elasticity for FSI problems is to combine the Eulerian perspective of the fluid model with the usual Lagrangian approach for the solid model, as described in [25]. To overcome this issue, we adopt a new splitting strategy, based on the Nitsche's method [23, 26, 27]. This approach separates the fluid from the structure sub-problems. We use finite elements for the spatial approximation and Backward Euler time stepping for time discretization. To reduce the computational cost, the coupled problem is split among its components and solved using a partitioned approach. We adopt a moving mesh algorithm, based on Arbitrary Lagrangian Eulerian (ALE) method to deal with moving domains.

We use the computational model to perform numerical experiments designed to elucidate the dynamic response of a poroelastic material under a variety of cyclic loading conditions. In particular, our study originates from [28] and [29] where the role of extracellular fluid flow in the apparent viscoelastic behavior of cardiac muscle was examined and the results confirmed that

a small hysteresis loop for the poroelastic model of myocardial tissue is observed for large deformations. As a result, we hypothesize that large deformations may trigger the effect of energy dissipation in the poroelastic materials. The simulations presented in this work show that there exists a range of loading conditions in which the poroelastic model is dissipative and a stress relaxation loop appears. There is rather little information on how energy loss (hysteresis etc.) depends on the rates of loading and deformation. The relative contributions of the fluid and solid phase effects (poroelasticity) have not been analyzed in detail. Our study brings some insight on these open questions by identifying the parameters for which energy dissipation is most relevant.

The manuscript is organized as follows. Section 2 deals with the description of constitutive framework for the interaction between the fluid and the poroelastic structure at finite strains. In Section 2.1, we present the partitioned algorithm to solve the fully discrete FPSI problem. In Section 4, we propose numerical simulations on the benchmark problems and discuss the numerical results in Section 5. Finally, conclusions are presented in Section 6.

2 Description of the problem

We study the flow in a channel bounded by a thick, compliant wall made of a poroelastic material. To this purpose, we consider a continuous medium in either two or three space dimensions, which occupies the domain $\Omega(t)$ in its deformed configuration. It is made of a free fluid in the region $\Omega_f(t)$ and of a deformable structure $\Omega_p(t)$ such that $\Omega_f(t) \cup \Omega_p(t) = \Omega(t)$, see Figure 1. We assume that the vessel is sufficiently large so that the non-Newtonian effects can be neglected. The fluid is modeled as an incompressible, viscous, Newtonian fluid using the Navier-Stokes equations. We study the time evolution of the domain and the velocity fields within the fluid and the structure.

The fluid model, namely the Navier-Stokes equation is written as:

$$\rho_f \left(\frac{\partial \boldsymbol{v}}{\partial t} + \boldsymbol{v} \cdot \nabla \boldsymbol{v} \right) = \nabla \cdot \boldsymbol{\sigma}_f \qquad in\ \Omega_f(t) \qquad (1)$$

$$\nabla \cdot \boldsymbol{v} = 0 \qquad in\ \Omega_f(t) \qquad (2)$$

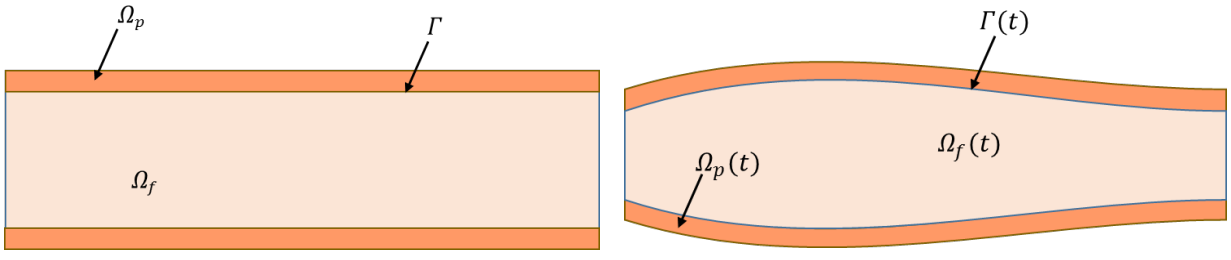

Figure 1. Geometric domain configurations, reference (left) and present (right)

Here, $\boldsymbol{v}$ and ρ_f stand for fluid velocity vector field and fluid density, respectively, and $\boldsymbol{\sigma}_f = -p_f \boldsymbol{I} + 2\mu_f \boldsymbol{D}(\boldsymbol{v})$ is the fluid Cauchy stress tensor where p_f is fluid pressure, μ_f is fluid dynamic viscosity and the symmetric part of fluid velocity gradient is defined as $\boldsymbol{D}(\boldsymbol{v}) = \frac{1}{2}(\nabla \boldsymbol{v} + \nabla \boldsymbol{v}^T)$.

We model the structure as a saturated poroelastic material. To this purpose, Biot's theory [30-33] is employed. However, since this theory was developed for soil consolidation, it not is considered to be completely adequate for describing the behavior of soft tissue. Indeed, several variants of it are available in literature, see for example [34], [35] and [36]. Here we consider as a reference model the general theory developed in [20] with a few simplifications. This formulation assumes that the porous material is consists of a mixture of fluid and solid phases. The solid material is assumed to be homogeneous in a macroscopic scale, and the pores to be interconnected. To simplify the model with respect to the general one of [20], we introduce the following hypotheses: *(i)* the inertial forces and the viscous forces are neglected in the momentum balance; *(ii)* we assume that constitutive relation for the porosity (i.e. the volume fraction of fluid) in terms of the pressure and the volumetric deformation of the solid phase is valid. Owing to the former assumption the fluid momentum equation simplifies as the Darcy's law of filtration. The latter assumption allows us to formulate the problem in terms of pore pressure p_p, displacement of the solid phase $\boldsymbol{U}$, and filtration velocity $\boldsymbol{q}$, defined as the relative velocity between the fluid and solid phases, multiplied by the porosity [37]. This set of unknowns is not the only admissible choice, but among other options, it makes it easier to formulate the coupling between the poroelastic model and the free flow model.

We choose a material configuration for the structural part of the domain. Let $\hat{x}$ denote a point in the material configuration $\widehat{\Omega}_p$ and let $\chi(t, \hat{x})$ be the deformation map, namely let x and $\hat{x}$ two corresponding point in the current and material configurations respectively, we have $x = \chi(t, \hat{x})$. Since the undeformed configuration $\hat{\Omega}$ is also the reference configuration for the structure, the structure velocity is equal to the material velocity. Based on this notation, the conservation laws for the structure are the following:

$$\frac{\partial \rho_p}{\partial t}|_{\hat{x}} = 0 \quad on\ \hat{\Omega}_p$$

$$\rho_p \frac{\partial^2 \boldsymbol{U}}{\partial t^2} - \widehat{\nabla} \cdot (\boldsymbol{P}) = 0 \quad in\ \hat{\Omega}_p$$

where $\widehat{\nabla}$ is the nabla operator with respect to the material coordinates in the reference domain. We denote by $\boldsymbol{F}$ the deformation gradient and its determinant is $J = \det(\boldsymbol{F})$. More precisely, let $d\hat{x}$ be a material element associated with the reference configuration that deforms into an element dx. Then, the fundamental relation $dx = \boldsymbol{F} \cdot d\hat{x}$ holds true. Here, $\boldsymbol{P}$ is the first Piola stress tensor defined as $\boldsymbol{P} = J\boldsymbol{\sigma}^P \boldsymbol{F}^{-T}$, $\boldsymbol{\sigma}^P$ denotes the poroelastic stress tensor and ρ_p is the poroelastic structure density. It is defined as $\boldsymbol{\sigma}^P = \boldsymbol{\sigma} - \alpha p_p \boldsymbol{I}$, where p_p is the fluid pressure inside the pores, $\boldsymbol{\sigma}$ is the Cauchy stress tensor and $\alpha \in (0,1]$ is the Biot modulus. Using the relationship

$\boldsymbol{\sigma}^P = J^{-1}\boldsymbol{F}\boldsymbol{S}^P\boldsymbol{F}^T$ between Cauchy stress in the porous media and the second Piola stress tensor for the poroelastic structure $\boldsymbol{S}^P = \boldsymbol{S} - \alpha J p_p \boldsymbol{C}^{-1}$, where $C = \boldsymbol{F}^T\boldsymbol{F}$, the model for the poroelastic wall in the Lagrangian/reference configuration $\hat{\Omega}_p$ becomes:

$$\rho_p \frac{\partial^2 \boldsymbol{U}}{\partial t^2} - \hat{\nabla} \cdot \left(\boldsymbol{F}\boldsymbol{S} - \alpha J p_p \boldsymbol{F}^{-T}\right) = 0 \qquad in\ \hat{\Omega}_p \qquad (3)$$

accounting for the momentum balance for the mixture, when the inertial forces of the fluid phase and the viscous effects are neglected, according to assumption (*i*). We use the St. Venant-Kirchhoff hyperelastic constitutive model for the solid matrix; for which the strain energy function is:

$$W = \frac{\lambda_p}{2} tr(\boldsymbol{\varepsilon}^2) + \mu_p \boldsymbol{\varepsilon} : \boldsymbol{\varepsilon} \qquad (4)$$

This yields the following expression for 2nd Piola stress tensor $\boldsymbol{S}$, where second order tensor $\boldsymbol{I}$ is the Kronecker delta function and $\boldsymbol{\varepsilon}(\boldsymbol{U})$ denotes the Green strain tensor,

$$\boldsymbol{S} = 2\mu_p \boldsymbol{\varepsilon}(\boldsymbol{U}) + \lambda_p \nabla \cdot \boldsymbol{U}\, \boldsymbol{I} \quad , \quad \boldsymbol{\varepsilon}(\boldsymbol{U}) = \frac{1}{2}(\nabla \boldsymbol{U} + \nabla \boldsymbol{U}^T + (\nabla \boldsymbol{U})\, \nabla \boldsymbol{U}^T)$$

In addition to equation (3), we consider Darcy's law for the fluid filling the pores,

$$k^{-1}\boldsymbol{q} = -\nabla p_p \qquad in\ \Omega_p(t) \qquad (5)$$

where the hydraulic conductivity of the porous matrix is *k* and it is assumed to be homogeneous. As mentioned in before, we eliminate the porosity from the equations of the system using assumption (*ii*). To this purpose, we adopt the constitutive relation used in [38], which can be formulated in terms of the density of added mass of the fluid, using the notation of [20],

$$m = \rho_f J\left(s_0 p_p + \alpha \nabla \cdot \boldsymbol{U}\right)$$

where α is the Biot modulus defined before and s_0 is the storage coefficient. This expression descends from the Athy's model for density, porosity and compaction of sedimentary rocks, see for example [39] for a review. However, a more thorough investigation of the adequacy of such models in the context of soft tissues is necessary. Replacing it into the mass conservation equation for the fluid phase and denoting by *D/Dt* ≡ D_t the material derivative we obtain,

$$\frac{D}{Dt}\left(s_0 p_p + \alpha \nabla \cdot \boldsymbol{U}\right) + \nabla \cdot \boldsymbol{q} = 0 \qquad in\ \ \Omega_p(t) \qquad (6)$$

The terms in the material derivative of equation (6) represent the action of pore and bulk compressibility on the flow. Pore compressibility is related to variations of porosity with pressure. The second term represents bulk compressibility, more precisely the compressibility of the bulk material. Later, we will say that the material is "nearly incompressible" to state that this

term is small. It should be noted that for the derivation of Biot system for a poroelastic material, i.e. equations (3), (5) and (6) the inertial and viscous forces in the fluid phase are assumed to be negligible. The effect of external forces such as gravity is neglected too. Therefore, the pore pressure is the dominant forcing term in the fluid flow through the poroelastic structure.

The fluid and poroelastic structure problems must be coupled by imposing some coupling conditions on the velocity, stress, and geometry over the interface between Ω_p and Ω_f, named Γ. We define normal and tangential unit vectors on $\partial\Omega_p$, $\partial\Omega_f$ and Γ. We denote by $\boldsymbol{n}_f$ the outward normal to the fluid domain and by $\boldsymbol{t}_f$ the corresponding tangential vector (note that we are implicitly using a two-dimensional notation, without any loss of generality for the model). This local coordinate system is also used on the interface Γ . Similarly, $\boldsymbol{n}_p, \boldsymbol{t}_p$ are the unit normal and tangential vectors on the boundary of Ω_p . Finally, we define $\boldsymbol{N}_p$ as the normal vector to the structure domain in the reference configuration and $\boldsymbol{T}_p$ as the corresponding tangential vector. Then, we require that,

$$\boldsymbol{v} \cdot \boldsymbol{t}_f = \frac{D\boldsymbol{U}}{Dt} \cdot \boldsymbol{t}_f \qquad on\ \Gamma(t) \tag{7}$$

$$\boldsymbol{v} \cdot \boldsymbol{n}_f = \left(\frac{D\boldsymbol{U}}{Dt} + \boldsymbol{q}\right) \cdot \boldsymbol{n}_f \qquad on\quad \Gamma(t) \tag{8}$$

$$\boldsymbol{n}_f \cdot \boldsymbol{\sigma}_f\, \boldsymbol{n}_f = -p_p \qquad on\quad \Gamma(t) \tag{9}$$

$$\boldsymbol{n}_f \cdot \boldsymbol{\sigma}_f\, \boldsymbol{n}_f - \boldsymbol{n}_f \cdot \boldsymbol{\sigma}_p \boldsymbol{n}_f = 0 \qquad on\quad \Gamma(t) \tag{10}$$

$$\boldsymbol{t}_f \cdot \boldsymbol{\sigma}_f\, \boldsymbol{n}_f - \boldsymbol{t}_f \cdot \boldsymbol{\sigma}_p \boldsymbol{n}_f = 0 \qquad on\quad \Gamma(t) \tag{11}$$

In equations (7) and (8), velocity continuity is enforced across the fluid-solid interface. In particular equation (8) describes the continuity of normal flux over the interface, which corresponds to the conservation of mass in the fluid phase. Balance of the normal components of stress in the fluid phase gives equation (9). Moreover, we ensure the balance of stresses on the interface in (11) and (10) for global conservation of momentum. We also have the kinematic constraint between the displacements of solid and fluid domains. It means that the velocity of the fluid domain coincides with the one of the structure at the interface:

$$\dot{\boldsymbol{U}} = \frac{D\boldsymbol{U}}{Dt} \qquad on\ \Gamma(t) \tag{12}$$

2.1 Variational formulation and energy balance

For the derivation of the variational formulation of the equations (3-6) we follow the approach already described in [23], with the main difference that here we consider finite deformations of the structure. To obtain the bilinear form for equation (3), we use the principle of minimum potential energy. The bilinear form relative to the pure elastic behavior of the structure is:

$$a_s(\boldsymbol{U}, \boldsymbol{\varphi}_p) := \int_{\widehat{\Omega}_p} \boldsymbol{F}\boldsymbol{S} : \nabla \boldsymbol{\varphi}_p \, d\hat{x} = \int_{\widehat{\Omega}_p} (I + \nabla \boldsymbol{U})\, \boldsymbol{S} : \nabla \boldsymbol{\varphi}_p \, d\hat{x} = \int_{\widehat{\Omega}_p} \boldsymbol{S} : D\boldsymbol{\varepsilon}(\boldsymbol{U})[\boldsymbol{\varphi}_p] \, d\hat{x} \quad (13)$$

Where with little abuse of notation $\boldsymbol{\varphi}_p$ denotes a test function in the material configuration.

Here, $D\boldsymbol{\varepsilon}(\boldsymbol{U})[\boldsymbol{\varphi}_p]$ is the Gateaux derivative of $\boldsymbol{\varepsilon}$ at $\boldsymbol{U}$ in the direction of $\boldsymbol{\varphi}_p$, namely

$$D\boldsymbol{\varepsilon}(\boldsymbol{U})[\boldsymbol{\varphi}_p] = \lim_{\Delta t \to 0} \frac{\boldsymbol{\varepsilon}(\boldsymbol{U} + \Delta t\, \boldsymbol{\varphi}_p) - \boldsymbol{\varepsilon}(\boldsymbol{U})}{\Delta t}$$
$$D\boldsymbol{\varepsilon}(\boldsymbol{U})[\boldsymbol{\varphi}_p] = \frac{1}{2}(\nabla \boldsymbol{\varphi}_p + \nabla \boldsymbol{\varphi}_p{}^T + \nabla \boldsymbol{\varphi}_p \, \nabla \boldsymbol{U}^T + \nabla \boldsymbol{U} \, \nabla \boldsymbol{\varphi}_p{}^T) \quad (14)$$

Also, we have:

$$b_s(p_p, \boldsymbol{\varphi}_p) := \alpha \int_{\widehat{\Omega}_p} J\, p_p \circ \chi^{-1}\, \boldsymbol{F}^{-T} : (\nabla \boldsymbol{\varphi}_p) d\hat{x} \quad (15)$$

where $\chi(t, \hat{x})$ is the deformation map in the domain $\widehat{\Omega}_p$. More precisely, the term $\hat{p}_p(\hat{x}, t) = p_p(\chi^{-1}(t, x), t) = p_p \circ \chi^{-1}$ defines the pressure in the reference domain. For the Darcy problem in a poroelastic medium we have two other terms, which account for the filtration through the porous matrix, equations (5)-(6) defined as:

$$a_p(\boldsymbol{q}, \boldsymbol{r}) := \int_{\Omega_p} \kappa^{-1}\, \boldsymbol{q} \cdot \boldsymbol{r} dx, \qquad b_p(p_p, \boldsymbol{r}) := \int_{\Omega_p} p_p \, \nabla \cdot \boldsymbol{r} dx$$

For the free flow equations (1)-(2), the trilinear and bilinear forms are:

$$a_f(\boldsymbol{v}, \boldsymbol{v}, \boldsymbol{\varphi}_f) := 2\mu_f \int_{\Omega_f} D(\boldsymbol{v}) : D(\boldsymbol{\varphi}_f) dx + \rho_f \int_{\Omega_f} (\boldsymbol{v} \cdot \nabla)\boldsymbol{v} \cdot \boldsymbol{\varphi}_f dx$$
$$b_f(p_f, \boldsymbol{\varphi}_f) := \int_{\Omega_f} p_f \, \nabla \cdot \boldsymbol{\varphi}_f dx$$

The forcing term for boundary conditions is:

$$F(t; \boldsymbol{\varphi}_f) = -\int_{\Gamma_f^{in}} p_{in}(t)\, \boldsymbol{\varphi}_f \cdot \boldsymbol{n}_f$$

In the process of deriving the previous bilinear forms from the governing equations, the Green's formula is applied. It makes the following interface terms appear in the variational formulation:

$$I_\Gamma = \int_\Gamma (\boldsymbol{\sigma}_f \boldsymbol{n}_f \cdot \boldsymbol{\varphi}_f - \boldsymbol{\sigma}_p \boldsymbol{n}_f \cdot \boldsymbol{\varphi}_p \circ \chi + p_p \boldsymbol{r} \cdot \boldsymbol{n}_f) \quad (16)$$

Using the interface conditions (9-11) we show that the previous term is equivalent to

$$I_\Gamma = \int_\Gamma \boldsymbol{\sigma}_f \boldsymbol{n}_f \cdot \left(\boldsymbol{\varphi}_f - \boldsymbol{\varphi}_p \circ \chi - \boldsymbol{r}\right) \cdot \boldsymbol{n}_f$$

Under the assumption that the solution of the system and the chosen test functions are regular enough, for any $t \in (0, T)$, the variational coupled fluid/solid problem consists to solve the following equation,

$$\begin{aligned}
&\rho_p \int_{\widehat{\Omega}_p} \partial_t \dot{\boldsymbol{U}} \cdot \boldsymbol{\varphi}_p d\hat{x} + \rho_p \int_{\widehat{\Omega}_p} (\dot{\boldsymbol{U}} - \partial_t \boldsymbol{U}) \cdot \dot{\boldsymbol{\varphi}}_p d\hat{x} \\
&+ a_s(\boldsymbol{U}, \boldsymbol{\varphi}_p) + \rho_f \int_{\Omega_f} \partial_t \boldsymbol{v} \cdot \boldsymbol{\varphi}_f dx + s_0 \int_{\Omega_p} D_t\, p_p \psi_p dx \\
&- b_s(p_p, \boldsymbol{\varphi}_p) + b_s(\psi_p, \partial_t \boldsymbol{U}) + a_p(\boldsymbol{q}, \boldsymbol{r}) - b_p(p_p, \boldsymbol{r}) + b_p(\psi_p, \boldsymbol{q}) \qquad (17) \\
&+ a_f(\boldsymbol{v}, \boldsymbol{v}, \boldsymbol{\varphi}_f) - b_f(p_f, \boldsymbol{\varphi}_f) + b_f(\psi_f, \boldsymbol{v}) \\
&\quad - I_\Gamma(\boldsymbol{v}, \boldsymbol{q}, p_f, p_p, \boldsymbol{U}; \boldsymbol{\varphi}_f, \boldsymbol{r}, \psi_f, \psi_p, \boldsymbol{\varphi}_p) = F(t; \boldsymbol{\varphi}_f)
\end{aligned}$$

Equation (17) naturally leads to the energy balance of the problem. Let us choose the following test functions $\boldsymbol{\varphi}_p = \partial_t \boldsymbol{U}$, $\dot{\boldsymbol{\varphi}}_p = \partial_t \dot{\boldsymbol{U}}$, $\boldsymbol{\varphi}_f = \boldsymbol{v}$, $\boldsymbol{r} = \boldsymbol{q}$, $\psi_f = p_f$, and $\psi_p = p_p$. We obtain that

$$\rho_f \int_{\Omega_f} \partial_t \boldsymbol{v} \cdot \boldsymbol{v}\, dx + a_f(\boldsymbol{v}, \boldsymbol{v}, \boldsymbol{v}) = \frac{d}{dt} \int_{\Omega_f(t)} \frac{\rho_f}{2} \boldsymbol{v}^2\, dx = \frac{d}{dt} K_f(t)\,,$$

being $K_f(t)$ the total kinetic energy of the fluid and

$$\rho_p \int_{\widehat{\Omega}_p} \partial_t \dot{\boldsymbol{U}} \cdot \partial_t \boldsymbol{U}\, d\hat{x} + \rho_p \int_{\widehat{\Omega}_p} (\dot{\boldsymbol{U}} - \partial_t \boldsymbol{U}) \cdot \partial_t \dot{\boldsymbol{U}}\, d\hat{x} = \frac{d}{dt} \int_{\widehat{\Omega}_p} \frac{\rho_p}{2} (\partial_t \boldsymbol{U})^2 d\hat{x} = \frac{d}{dt} K_p(t)\,,$$

being $K_p(t)$ the kinetic energy of the porous matrix.

Following standard arguments of the mechanics of continua [40], we have,

$$a_s(\boldsymbol{U}, \partial_t \boldsymbol{U}) = \int_{\widehat{\Omega}_p} \boldsymbol{S} : D\boldsymbol{\varepsilon}(\boldsymbol{U})[\partial_t \boldsymbol{U}]\, d\hat{x} = \frac{d}{dt} \int_{\widehat{\Omega}_p} \boldsymbol{S} : D\boldsymbol{\varepsilon}(\boldsymbol{U})[\boldsymbol{U}]\, d\hat{x} = \frac{d}{dt}\, \varepsilon_p(t)$$

where $\varepsilon_p(t) = \int_{\widehat{\Omega}_p} W$ is the total stored energy of the porous matrix. We notice that the bilinear forms b_s , b_f , b_p cancel out because of the choice of the test functions, and that for the same reason $I_\Gamma(\boldsymbol{v}, \boldsymbol{q}, p_f, p_p, \boldsymbol{U}_h; \boldsymbol{v}, \boldsymbol{q}, p_f, p_p, \partial_t \boldsymbol{U}) = 0$.

Putting together the previous results, after integration in time from $t = 0$ to $t = T$, we obtain the following equation of the energy balance:

$$K_f(T) + K_p(T) + \varepsilon_p(T) + \int_0^T \int_{\Omega_f(t)} 2\mu_f(D(\boldsymbol{v}))^2 + \int_{\Omega_p(t)} \frac{1}{2}\left(S_0\left(p_p\right)^2\right) + \int_0^T \int_{\Omega_p(t)} k^{-1}(\boldsymbol{q})^2 = K_f(0) + K_p(0) + \varepsilon_p(0) + \int_{\Omega_p(0)} \frac{1}{2}\left(S_0\left(p_p\right)^2\right) \quad (18)$$

This equation shows that the viscous forces in the free fluid, proportional to μ_f, as well as the friction effect due to the motion of fluid through the porous medium, which is proportional to k^{-1} are the main dissipation sources of the system. More precisely, the latter dissipation term appears in the Darcy equation. However, this effect is also transferred to the momentum balance of the solid phase, according to the action-reaction principle, by means of the pressure term of equation (3), namely $\alpha J p_p \boldsymbol{F}^{-T}$.

3 Numerical discretization

For fluid-porous-solid interaction, a two-way coupled model is used, wherein the fluid flow and the solid deformations mutually affect each other. A common approach to dealing with this problem is to separate the two models and solve each one independently by means of an iterative loop. The two algorithms communicate through the coupling conditions on the interface. Solving the uncoupled sub-problems, sequentially for multiple times, is referred to as a "partitioned approach". Nitsche's method is an effective technique for enforcing boundary and interface conditions at the discrete level, in the framework of the finite element method [27]. It has been used for enforcing the interface conditions between non-conforming meshes in the fluid and structure domains [26]. The application of Nitsche's method to a FSI problem is provided in [26, 41] and has been applied in a similar manner for FPSI system in [23] for enforcing interface conditions. In the latter study, the interface conditions (7)-(11) appear in the variational formulation in a modular form. Therefore, it is straightforward to design a partitioned algorithm to solve each equation of the problem independently using time lagging.

We adopt the ALE formulation for the free fluid, together with a Lagrangian frame for the poroelastic structure. This yields an FPSI problem that is composed by four sub-problems, namely the free fluid problem, which allows for the computation of the velocity and pressure inside the free fluid domain, the structure problem, which describes the deformation of the vessel wall, the Darcy problem, which allows for the computation of the velocity and pressure inside the porous medium and the ALE map update, which accounts for the evolution of the domain.

To combine the Eulerian and the Lagrangian setting required for describing FPSI we use in the domain Ω_p the deformation mapping χ (already defined before). In the domain Ω_f , with little

abuse of notation, we sill use the symbol χ for the ALE mapping. We define χ^{-1} as the inverse of mapping χ. Then, using χ or χ^{-1}on a variable or its corresponding test function, means pulling-forward or pushing-back between reference and current domains.

3.1 Spatial discretization using finite elements

The finite element method (FEM) is applied to solve the coupled system of equations. We denote with $\boldsymbol{V}_h^f, \boldsymbol{Q}_h^f$ the finite element spaces for the velocity and pressure approximation on the fluid domain Ω_f, with $\boldsymbol{V}_h^p, \boldsymbol{Q}_h^p$ the spaces for velocity and pressure approximation of the porous domain Ω_p and with $\boldsymbol{X}_h^p, \dot{\boldsymbol{X}}_h^p$ the approximation spaces for the structure displacement and velocity, respectively. We define test functions $\boldsymbol{\varphi}_{f,h}, \psi_{f,h}, \boldsymbol{r}_h, \psi_{p,h} \in \boldsymbol{V}_h^f \times \boldsymbol{Q}_h^f \times \boldsymbol{V}_h^p \times \boldsymbol{Q}_h^p$ and $\boldsymbol{\varphi}_{p,h}, \dot{\boldsymbol{\varphi}}_{p,h} \in \boldsymbol{X}_h^p \times \dot{\boldsymbol{X}}_h^p$. We assume that all the finite element approximation spaces comply with the prescribed Dirichlet conditions on external boundaries $\partial\Omega_f$, $\partial\Omega_p$. However, we do not require that the discrete spaces satisfy the kinematic interface conditions, namely equations (7-8). We enforce these conditions weakly, using Nitsche's method. More precisely, starting from the expression of I_Γ, Nitsche's method allows us to weakly enforce the interface conditions (7)-(11), we remand the interested reader to [23] for details, such that (16) becomes:

$$
\begin{aligned}
I_\Gamma^* + S_\Gamma^{*,\varsigma} = & -\int_\Gamma \boldsymbol{n}_f \cdot \boldsymbol{\sigma}_{f,h}(\boldsymbol{v}_h, p_{f,h})\boldsymbol{n}_f \, (\boldsymbol{\varphi}_{f,h} - \boldsymbol{r}_h - \boldsymbol{\varphi}_{p,h} \circ \chi) \cdot \boldsymbol{n}_f \\
& -\int_\Gamma \boldsymbol{n}_f \cdot \boldsymbol{\sigma}_{f,h}(\varsigma\boldsymbol{\varphi}_{f,h}, -\psi_{f,h})\boldsymbol{n}_f \, (\boldsymbol{v}_h - \boldsymbol{q}_h - D_t\boldsymbol{U}_h) \cdot \boldsymbol{n}_f \\
& +\int_\Gamma \gamma_f \, \mu_f h^{-1} \Big((\boldsymbol{v}_h - \boldsymbol{q}_h - D_t\boldsymbol{U}_h) \\
& \quad \cdot \boldsymbol{n}_f \Big) \Big((\boldsymbol{\varphi}_{f,h} - \boldsymbol{r}_h - \boldsymbol{\varphi}_{p,h} \circ \chi) \cdot \boldsymbol{n}_f \Big) \\
& +\int_\Gamma \gamma_f \, \mu_f h^{-1} \, (\boldsymbol{v}_h - D_t\boldsymbol{U}_h) \cdot \boldsymbol{t}_f \, (\boldsymbol{\varphi}_{f,h} - \boldsymbol{\varphi}_{p,h} \circ \chi) \cdot \boldsymbol{t}_f
\end{aligned}
\tag{19}
$$

Here h denotes the characteristic size of the computational mesh. More precisely, we assume that the computational meshes of Ω_f and Ω_p are conforming on Γ. We also assume the mesh characteristic sizes in the reference and current configurations are comparable and they are both denoted by h. For the problem on Ω_f we introduce $\boldsymbol{w}_h$, that is the ALE velocity, namely the time derivative of the ALE map χ, required to deform the fluid domain in a way that it always matches the structure. Then, the semi-discrete coupled fluid/solid problem consists to solve the following equation,

$$
\begin{aligned}
& \rho_p \int_{\hat{\Omega}_p} \partial_t \, \dot{\boldsymbol{U}}_h \cdot \boldsymbol{\varphi}_{p,h} d\hat{x} + \rho_p \int_{\hat{\Omega}_p} (\dot{\boldsymbol{U}}_h - \partial_t \boldsymbol{U}_h) \cdot \dot{\boldsymbol{\varphi}}_{p,h} d\hat{x} \\
& + a_s(\boldsymbol{U}_h, \boldsymbol{\varphi}_{p,h}) + \rho_f \int_{\Omega_f} \partial_t \, \boldsymbol{v}_h \cdot \boldsymbol{\varphi}_{f,h} dx + s_0 \int_{\Omega_p} D_t \, p_{p,h} \psi_{p,h} dx
\end{aligned}
\tag{20}
$$

$$
\begin{aligned}
&-b_s(p_{p,h}, \boldsymbol{\varphi}_{p,h}) + b_s(\psi_{p,h}, \partial_t \boldsymbol{U}_h) + a_p(\boldsymbol{q}_h, \boldsymbol{r}_h) - b_p(p_{p,h}, \boldsymbol{r}_h) \\
&+b_p(\psi_{p,h}, \boldsymbol{q}_h) + a_f(\boldsymbol{v}_h - \boldsymbol{w}_h, \boldsymbol{v}_h, \boldsymbol{\varphi}_{f,h}) - b_f(p_{f,h}, \boldsymbol{\varphi}_{f,h}) \\
&+b_f(\psi_{f,h}, \boldsymbol{v}_h) \\
&-(I_\Gamma^* + S_\Gamma^{*,\varsigma})(\boldsymbol{v}_h, \boldsymbol{q}_h, p_{f,h}, p_{p,h}, \boldsymbol{U}_h; \boldsymbol{\varphi}_{f,h}, \boldsymbol{r}_h, \psi_{f,h}, \psi_{p,h}, \boldsymbol{\varphi}_{p,h}) \\
&= F(t; \boldsymbol{\varphi}_{f,h})
\end{aligned}
$$

In what follows we describe the decomposition of problem (20) into sub-problems, performed at the same time of the numerical discretization. In this way, we obtain a loosely coupled scheme for the decomposition of the structure and fluid problems. As described in the following sub-sections, the loosely coupled scheme consists of solving sequentially (without sub-iterations) the structure problem, the Darcy equations and finally the Navier-Stokes equations.

3.2 Structure problem

First, we preform the time discretization by means of finite differences. Let Δt denotes the time step, $t_n = n\Delta t$, $0 \le n \le N$, and let the first order (backward) discrete time derivative be defined as:

$$
d_\tau \boldsymbol{U}^n := \frac{\boldsymbol{U}^n - \boldsymbol{U}^{n-1}}{\Delta t}
$$

It should be noted that in the time discrete scheme we replace the term $\partial_t \dot{\boldsymbol{U}}_h$ with the three-point finite difference approximation of the second-order derivative of the displacement, namely:

$$
d_\tau \dot{\boldsymbol{U}}^n := \frac{\boldsymbol{U}^n - 2\boldsymbol{U}^{n-1} + \boldsymbol{U}^{n-2}}{\Delta t^2}
$$

Given $\boldsymbol{v}_h^{n-1}, p_{f,h}^{n-1}, \boldsymbol{q}_h^{n-1}, p_{p,h}^{n-1}$ find $\boldsymbol{U}_h^n$ in $\hat{\Omega}_p$ such that we have (21):

$$
\begin{aligned}
&\frac{\rho_p}{\Delta t^2} \int_{\hat{\Omega}_p} (\boldsymbol{U}_h^n - 2\boldsymbol{U}_h^{n-1} + \boldsymbol{U}_h^{n-2}) \cdot \boldsymbol{\varphi}_{p,h} \, d\hat{x} \\
&+ \int_{\hat{\Omega}_p} \boldsymbol{S}(\boldsymbol{\varepsilon}(\boldsymbol{U}_h^n)) : D\boldsymbol{\varepsilon}(\boldsymbol{U}_h^n)[\boldsymbol{\varphi}_{p,h}] \, d\hat{x} + \int_{\hat{\Gamma}} \gamma_f \, \mu_f h^{-1} (d_\tau \boldsymbol{U}_h^n \cdot \boldsymbol{T}_p)(\boldsymbol{\varphi}_{p,h} \cdot \boldsymbol{T}_p) \\
&+ \int_{\hat{\Gamma}} \gamma_f \, \mu_f h^{-1} (d_\tau \boldsymbol{U}_h^n \cdot \boldsymbol{N}_p)(\boldsymbol{\varphi}_{p,h} \cdot \boldsymbol{N}_p) - \int_{\hat{\Gamma}} J\chi^{-1}(\boldsymbol{\sigma}_{f,h}^{n-1}) \, \boldsymbol{F}^{-T} \boldsymbol{N}_p \, \boldsymbol{\varphi}_{p,h} \qquad (21) \\
&= b_s(p_{p,h}^{n-1}, \boldsymbol{\varphi}_{p,h}) + \int_{\hat{\Gamma}} \gamma_f \, \mu_f h^{-1} \chi^{-1}(\boldsymbol{v}_h^{n-1}) \cdot \boldsymbol{T}_p \, (\boldsymbol{\varphi}_{p,h} \cdot \boldsymbol{T}_p) \\
&+ \int_{\hat{\Gamma}} \gamma_f \, \mu_f h^{-1} \chi^{-1}(\boldsymbol{v}_h^{n-1} - \boldsymbol{q}_h^{n-1}) \cdot \boldsymbol{N}_p \, (\boldsymbol{\varphi}_{p,h} \cdot \boldsymbol{N}_p)
\end{aligned}
$$

Since both the deformation gradient $\boldsymbol{F}$ and the 2nd Piola stress tensor $\boldsymbol{S}$ in the bilinear form a_s depend on the displacement of the structure $\boldsymbol{U}$, the finite element discretization of the structure problem leads to a system of non-linear equations. It is solved iteratively by the Newton method (similar to the approach used in [42], [7] and [43].

3.2.1 **Newton's method**

We describe, a Newton-type (also known as Newton-Raphson) iterative strategy to solve the residual equation at each time step. This algorithm consists of the following steps:

1) Given $\boldsymbol{v}_h^{n-1}, p_{f,h}^{n-1}, \boldsymbol{q}_h^{n-1}, p_{p,h}^{n-1}$, solve the linearized equations to find the incremental displacement $\Delta\boldsymbol{U}^k$ in $\hat{\Omega}_p$ such that: $a_s{}^*\big(\boldsymbol{U}^k, \Delta\boldsymbol{U}^k, \boldsymbol{\varphi}_p\big) = a\big(\boldsymbol{U}^k, \boldsymbol{\varphi}_p\big) - L\big(\boldsymbol{\varphi}_p\big)$

2) Update the displacement $\boldsymbol{U}^{k+1} = \boldsymbol{U}^k - \Delta\boldsymbol{U}^k$

3) Exit the loop if $\|\Delta\boldsymbol{U}^k\| \leq epsilon$

Here $a_s{}^*\big(\boldsymbol{U}, \Delta\boldsymbol{U}, \boldsymbol{\varphi}_p\big)$ denotes the linearization of $a_s\big(\boldsymbol{U}, \boldsymbol{\varphi}_p\big)$, that is:

$$
\begin{aligned}
a_s{}^*\big(\boldsymbol{U}, \Delta\boldsymbol{U}, \boldsymbol{\varphi}_p\big) &= \int_{\hat{\Omega}_p} \boldsymbol{\mathcal{C}} : D\boldsymbol{\varepsilon}(\boldsymbol{U})\big[\boldsymbol{\varphi}_p\big] : D\boldsymbol{\varepsilon}(\boldsymbol{U})[\Delta\boldsymbol{U}]\, d\hat{x} \\
&\quad + \int_{\hat{\Omega}_p} \boldsymbol{S}\big(\boldsymbol{\varepsilon}(\boldsymbol{U})\big) : D^2\boldsymbol{\varepsilon}(\boldsymbol{U})\big[\boldsymbol{\varphi}_p, \Delta\boldsymbol{U}\big] d\hat{x} \\
&= \int_{\hat{\Omega}_p} \boldsymbol{\mathcal{C}} : D\boldsymbol{\varepsilon}(\boldsymbol{U})\big[\boldsymbol{\varphi}_p\big] : D\boldsymbol{\varepsilon}(\boldsymbol{U})[\Delta\boldsymbol{U}]\, d\hat{x} \\
&\quad + \int_{\hat{\Omega}_p} \boldsymbol{\mathcal{C}} : \boldsymbol{\varepsilon}(\boldsymbol{U}) : D^2\boldsymbol{\varepsilon}(\boldsymbol{U})\big[\boldsymbol{\varphi}_p, \Delta\boldsymbol{U}\big] d\hat{x}
\end{aligned}
\tag{22}
$$

Now we specify tensors $\boldsymbol{\mathcal{C}}, D\boldsymbol{\varepsilon}(\boldsymbol{U}), D^2\boldsymbol{\varepsilon}(\boldsymbol{U})$. Tensor $\boldsymbol{\mathcal{C}}$ is the Lagrangian elasticity tensor defined as:

$$\boldsymbol{\mathcal{C}}_{ijkl} = \lambda_p \delta_{ij}\delta_{kl} + \mu_p(\delta_{ik}\delta_{jl} + \delta_{il}\delta_{jk})$$

from which we obtain,

$$\boldsymbol{\mathcal{C}} = \begin{bmatrix} 2\mu_p + \lambda_p & 0 & \lambda_p \\ 0 & \mu_p & 0 \\ \lambda_p & 0 & 2\mu_p + \lambda_p \end{bmatrix}$$

Using expression for $D\boldsymbol{\varepsilon}(\boldsymbol{U})$ given (14), $D^2\boldsymbol{\varepsilon}(\boldsymbol{U})$ takes the following expressions:

$$D^2\boldsymbol{\varepsilon}(\boldsymbol{U})\left[\boldsymbol{\varphi}_p, \Delta\boldsymbol{U}\right] = \frac{1}{2}(\nabla\boldsymbol{\varphi}_p\,\nabla\boldsymbol{U}^T + \nabla\boldsymbol{U}\,\nabla{\boldsymbol{\varphi}_p}^T)$$
$$D^2\boldsymbol{\varepsilon}(\boldsymbol{U})\left[\boldsymbol{\varphi}_p, \Delta\boldsymbol{U}\right] = \lim_{\Delta t\to 0}\frac{D\boldsymbol{\varepsilon}(\boldsymbol{U}+\Delta t\,\Delta\boldsymbol{U})[\boldsymbol{\varphi}_p] - D\boldsymbol{\varepsilon}(\boldsymbol{U})[\boldsymbol{\varphi}_p]}{\Delta t} \tag{23}$$

Then, the linearized equations consist of finding $\Delta\boldsymbol{U}^k$ in $\widehat{\Omega}_p$ such that:

$$\begin{aligned}
&\frac{\rho_p}{\Delta t^2}\int_{\widehat{\Omega}_p}\Delta\boldsymbol{U}^k\cdot\boldsymbol{\varphi}_{p,h}\,d\hat{x} + \int_{\widehat{\Omega}_p}\boldsymbol{\mathcal{C}}\colon D\boldsymbol{\varepsilon}\left(\boldsymbol{U}_h^{nk}\right)\left[\boldsymbol{\varphi}_{p,h}\right]\colon D\boldsymbol{\varepsilon}\left(\boldsymbol{U}_h^{nk}\right)[\Delta\boldsymbol{U}^k]\,d\hat{x}\\
&+\int_{\widehat{\Omega}_p}\boldsymbol{S}\left(\boldsymbol{\varepsilon}\left(\boldsymbol{U}_h^{nk}\right)\right)\colon D^2\boldsymbol{\varepsilon}\left(\boldsymbol{U}_h^{nk}\right)\left[\boldsymbol{\varphi}_{p,h},\Delta\boldsymbol{U}^k\right]d\hat{x}\\
&-\frac{\rho_p}{\Delta t^2}\int_{\widehat{\Omega}_p}\left(\boldsymbol{U}_h^{nk}-2\boldsymbol{U}_h^{n-1}+\boldsymbol{U}_h^{n-2}\right)\cdot\boldsymbol{\varphi}_{p,h}d\hat{x}\\
&-\int_{\widehat{\Omega}_p}\boldsymbol{S}\left(\boldsymbol{\varepsilon}\left(\boldsymbol{U}_h^{nk}\right)\right)\colon D\boldsymbol{\varepsilon}\left(\boldsymbol{U}_h^{nk}\right)[\boldsymbol{\varphi}_s]\,d\hat{x} - \int_{\widehat{\Gamma}}\gamma_f\,\mu_f h^{-1}d_\tau\boldsymbol{U}_h^{nk}\cdot\left(\boldsymbol{\varphi}_{p,h}\right)\\
&+\int_{\widehat{\Gamma}}J(\boldsymbol{\sigma}_{f,h}^{n-1}\circ\chi^{-1})\,\boldsymbol{F}^{-T}\boldsymbol{N}_p\left(\boldsymbol{\varphi}_{p,h}\right) + b_s\left(p_{p,h}^{n-1},\boldsymbol{\varphi}_{p,h}\right)\\
&+\int_{\widehat{\Gamma}}\gamma_f\,\mu_f h^{-1}(\boldsymbol{v}_h^{n-1}\circ\chi^{-1})\cdot\boldsymbol{T}_p\left(\boldsymbol{\varphi}_{p,h}\cdot\boldsymbol{T}_p\right)\\
&+\int_{\widehat{\Gamma}}\gamma_f\,\mu_f h^{-1}\left((\boldsymbol{v}_h^{n-1}-\boldsymbol{q}_h^{n-1})\right)\circ\chi^{-1}\cdot\boldsymbol{N}_p\left(\boldsymbol{\varphi}_{p,h}\cdot N_p\right)=0
\end{aligned} \tag{24}$$

3.3 Darcy problem

Adopting the same time discretization method used for the structure problem, given $\boldsymbol{v}_h^{n-1}, p_{f,h}^{n-1}$ and $\boldsymbol{U}_h^n$, the fully discrete Darcy problem consists of finding $\boldsymbol{q}_h^n, p_{p,h}^n$ in ${\Omega_p}^{n-1}$ such that:

$$\begin{aligned}
&s_0\int_{{\Omega_p}^{n-1}}d_\tau\,p_{p,h}^n\psi_{p,h}dx\; + a_p(\boldsymbol{q}_h^n,\boldsymbol{r}_h) - b_p\left(p_{p,h}^n,\boldsymbol{r}_h\right)\\
&+b_p\left(\psi_{p,h},\boldsymbol{q}_h^n\right) + \int_{\Gamma^{n-1}}\gamma_f\,\mu_f h^{-1}\left(\boldsymbol{q}_h^n\cdot\boldsymbol{n}_p\right)\left(\boldsymbol{r}_h\cdot\boldsymbol{n}_p\right)\\
&+s_{f,\boldsymbol{q}}\left(d_\tau\boldsymbol{q}_h\cdot\boldsymbol{n}_p,\boldsymbol{r}_h\cdot\boldsymbol{n}_p\right)\\
&=-b_s\left(\psi_{p,h},d_\tau\boldsymbol{U}_h^n\right)
\end{aligned} \tag{25}$$

$$+\int_{\Gamma^{n-1}}\gamma_f\,\mu_f h^{-1}\left((\boldsymbol{v}_h^{n-1}-d_\tau\boldsymbol{U}_h^{n-1})\cdot\boldsymbol{n}_p\right)\left(\boldsymbol{r}_h\cdot\boldsymbol{n}_p\right)$$

$$+\int_{\Gamma^{n-1}}\left(\boldsymbol{n}_p\cdot\boldsymbol{\sigma}_{f,h}^{n-1}\boldsymbol{n}_p\right)\left(\boldsymbol{r}_h\cdot\boldsymbol{n}_p\right).$$

Based on the conditions (10), the pressure in the porous media p_p^n has been replaced by the normal component of stress in the fluid phase $\boldsymbol{\sigma}_{f,h}^{n-1}$, computed at the previous time step to improve stability. We also introduce new stabilization term, which is discussed in [11, 23]:

$$s_{f,q}(d_\tau\boldsymbol{q}_h^n\cdot\boldsymbol{n}_p,\boldsymbol{r}_h\cdot\boldsymbol{n}_p)=\gamma'_{stab}\gamma_f\mu_f\frac{\Delta t}{h}\int_{\Gamma^{n-1}}\left(d_\tau\boldsymbol{q}_h^n\cdot\boldsymbol{n}_p\right)\left(\ \boldsymbol{r}_h\cdot\boldsymbol{n}_p\right),$$

3.4 Fluid problem

The space and time discrete version of the Navier-Stokes equations for blood flow in the artery are solved as the third step of the loosely coupled scheme. Given $\boldsymbol{q}_h^n, p_{p,h}^n, \boldsymbol{U}_h^n$, we aim to find $\boldsymbol{v}_h^n, p_{f,h}^n$ in ${\Omega_f}^{n-1}$ such that:

$$\begin{aligned}
&\rho_f\int_{{\Omega_f}^n}\boldsymbol{v_h^n}\cdot\boldsymbol{\varphi}_{f,h}dx+a_f\left(\boldsymbol{v}_h^{n-1}-\boldsymbol{w}_h^{n-1},\boldsymbol{v}_h^n,\boldsymbol{\varphi}_{f,h}\right)-b_f\left(p_{f,h}^n,\boldsymbol{\varphi}_{f,h}\right)\\
&+b_f\left(\psi_{f,h},\boldsymbol{v}_h^n\right)+s_{f,p}\left(d_\tau p_{f,h},\psi_{f,h}\right)+s_{f,v}\left(d_\tau\boldsymbol{v}_h^n\cdot\boldsymbol{n}_f,\boldsymbol{\varphi}_{f,h}\cdot\boldsymbol{n}_f\right)\\
&-\int_{\Gamma^{n-1}}\boldsymbol{\sigma}_{f,h}\left(\varsigma\boldsymbol{\varphi}_{f,h},-\psi_{f,h}\right)\boldsymbol{n}_f\cdot\boldsymbol{v}_h^n+\int_{\Gamma^{n-1}}\gamma_f\,\mu_f h^{-1}\boldsymbol{v}_h^n\cdot\boldsymbol{\varphi}_{f,h}\\
&=\rho_f\int_{{\Omega_f}^{n-1}}\boldsymbol{v_h^{n-1}}\cdot\boldsymbol{\varphi}_{f,h}dx\\
&-\int_{{\Gamma_f^{in}}^{n-1}}p_{in}\,(t)\,\boldsymbol{\varphi}_f\cdot\boldsymbol{n}_f+\int_{\Gamma^{n-1}}\boldsymbol{\sigma}_{f,h}^{n-1}\,\boldsymbol{n}_f\cdot\boldsymbol{\varphi}_{f,h}\\
&-\int_{\Gamma^{n-1}}\left(\boldsymbol{t}_f\cdot\boldsymbol{\sigma}_{f,h}\left(\varsigma\boldsymbol{\varphi}_{f,h},-\psi_{f,h}\right)\boldsymbol{n}_f\right)(d_\tau\boldsymbol{U}_h^n\circ\chi)\cdot\boldsymbol{t}_f\\
&-\int_{\Gamma^{n-1}}\left(\boldsymbol{n}_f\cdot\boldsymbol{\sigma}_{f,h}\left(\varsigma\boldsymbol{\varphi}_{f,h},-\psi_{f,h}\right)\boldsymbol{n}_f\right)\left(\boldsymbol{q}_h^n+(d_\tau\boldsymbol{U}_h^n\circ\chi)\right)\cdot\boldsymbol{n}_f\\
&+\int_{\Gamma^{n-1}}\gamma_f\,\mu_f h^{-1}\left(\boldsymbol{q}_h^n+(d_\tau\boldsymbol{U}_h^n\circ\chi)\right)\cdot\boldsymbol{n}_f\left(\boldsymbol{\varphi}_{f,h}\cdot\boldsymbol{n}_f\right)\\
&+\int_{\Gamma^{n-1}}\gamma_f\,\mu_f h^{-1}\left((d_\tau\boldsymbol{U}_h^n\circ\chi)\cdot\boldsymbol{t}_f\right)\left(\boldsymbol{\varphi}_{f,h}\cdot\boldsymbol{t}_f\right).
\end{aligned}\tag{26}$$

Here $s_{f,p}(d_\tau p_{f,h}, \psi_{f,h})$ is a stabilization term proposed in [11, 23] acting on the free fluid pressure, that helps to restore the stability of the explicit time advancing scheme, and the role of $s_{f,\boldsymbol{v}}$ is to control the increment of $\boldsymbol{v}_h^n$ over two subsequent time steps, namely we have:

$$s_{f,p}(d_\tau p_{f,h}, \psi_{f,h}) = \gamma_{stab} \frac{h\Delta t}{\gamma_f \mu_f} \int_{\Gamma^{n-1}} d_\tau \, p_{f,h}^n \, \psi_{f,h} \tag{27}$$

$$s_{f,v}(d_\tau \boldsymbol{v}_h^n \cdot \boldsymbol{n}_f, \boldsymbol{\varphi}_{f,h} \cdot \boldsymbol{n}_f) = \gamma'_{stab} \gamma_f \mu_f \frac{\Delta t}{h} \int_{\Gamma^{n-1}} \left(d_\tau \boldsymbol{v}_h^n \cdot \boldsymbol{n}_f\right) \left(\boldsymbol{\varphi}_{f,h} \cdot \boldsymbol{n}_f\right) \tag{28}$$

3.5 Mesh movement

Knowing the displacement of the structure interface, the harmonic extension approach has been proposed to update the fluid mesh of the fluid–structure interaction problem [44]. A similar procedure has been used for updating the computational mesh for the Darcy problem. Let $\boldsymbol{w}$ be the mesh deformation velocity from the reference configuration, also called the ALE velocity, and η be the diffusion coefficient [6]. The idea is to harmonically extend the evolution of the boundary onto the whole of $\hat{\Omega}_f$:

$$\nabla.(\eta \nabla \boldsymbol{w}) = 0 \qquad in\ \hat{\Omega}_f \tag{29}$$

It is common to consider the diffusion coefficient as a constant [9]. In the numerical tests of this chapter, we assume η =1 and we solve for (30):

$$\begin{aligned} \nabla^2 \boldsymbol{w} &= 0 && in\ \hat{\Omega}_f \\ \boldsymbol{w} \cdot \boldsymbol{n}_f &= 0 && on\ \partial\hat{\Omega}_f \setminus \hat{\Gamma}\ \ , \hat{\Gamma}_f^{in}\ and\ \hat{\Gamma}_f^{out} \\ \boldsymbol{w} &= d\boldsymbol{U}/dt && on\ \hat{\Gamma} = \hat{\Omega}_f \cap \hat{\Omega}_p \end{aligned} \tag{30}$$

Given the ALE velocity, we calculate the ALE map from time step $n-1$ to step n as follows

$$\chi^n = \chi^{n-1} + \boldsymbol{w}\Delta t$$

This operation allows us to update the domains from $\Omega_f^{n-1}, \Omega_p^{n-1}$ to Ω_f^n, Ω_p^n . Since we do not change the mesh topology (i.e. we do not re-mesh) from one iteration to the following, it is also straightforward to update the variables calculated on the domains $\Omega_f^{n-1}, \Omega_p^{n-1}$ to the current ones, namely Ω_f^n, Ω_p^n. It is also straightforward to determine what is the position on the reference domain of a node on the current fluid domain. In this way, we determine the discrete version of the map χ^{-1}.

4 Numerical Simulations

In this section, we discuss some numerical experiments to study the behavior of soft biological tissue subject to cyclic loads, using the FPSI algorithm developed in the previous section. We have implemented the mathematical methods described previously, into a numerical solver. For the spatial approximation of the fluid and structure equations, we exploit the finite element method. In order to achieve a stable discretization of the divergence- free constraint, we use *inf-sup* stable mixed finite elements, i.e. P2-P1 approximation of the velocity and pressure fields, respectively, for both Navier-Stokes and Darcy equations. Porous matrix displacement is discretized using P2 finite elements. The systems of algebraic equations arising from the finite element method are solved by means of a direct method. For the stopping criterion for the Newton's method, tolerance of 1.e-5 is applied. For the time discretization, we use Backward Euler finite differences. Due to the fast dynamics of the solution and semi-implicit treatment of the fluid convective term ($\boldsymbol{v}^{n+1}.\nabla\boldsymbol{v}^{n+1} \approx \boldsymbol{v}^{n}.\nabla\boldsymbol{v}^{n+1}$), we have to use very small time step (Δt=1.e-5 sec, is used). All computations have been performed using an in house finite element solver, coded using the Freefem++ library [45]. For the stabilization of the convection dominated flow in Ω_f, the SUPG method is employed [46]. We perform numerical experiments on idealized geometries that represent blood-tissue systems. Benchmark problem 1 shows the ability of our proposed methodology to capture the large deformations in the FPSI problem and is motived by the interaction between the blood flow and the wall of large arteries. Next, the proposed methodology is used in benchmark problem 2 to study the energy dissipation in the FPSI framework. The geometrical model in this example resembles a 2D model of the left ventricle (LV), similar to the simplified LV model, presented in [47] .

4.1 Benchmark Example 1 : Simulation of the flow in a compliant vessel

Our first test case is a variant of the classical FSI benchmark problem that has been used in several works [41, 48]. The geometry consists of a 2D straight pipe that can be seen as an idealized portion of the descending of aorta. The problem consists in studying the propagation of a single pressure wave with amplitude comparable to the pressure difference between systolic and diastolic phases of the heartbeat. In particular, the following time-dependent inflow pressure profile is prescribed, where p_{max} = 13334 dyne/cm^2 and T_{max} = 0.003 s.

$$p_{in}(t) = \begin{cases} \frac{p_{max}}{2}\left(1-\cos\left(\frac{2\pi t}{T_{max}}\right)\right) & if\ \ t \le T_{max} \\ 0 & if\ \ t > T_{max} \end{cases} \tag{31}$$

At the outflow, we prescribe homogeneous (traction-free) Neumann type boundary condition. The physical parameters used in this study fall within the range of physiological values for the blood flow and are reported in Table 1. For implementation details and the visualization of the wall displacement at different time points, reader is referred to our previous study [23].

Table 1. Physical and numerical parameters for benchmark problem 1

Parameters	values	Parameters	values
R_i (cm)	0.5	Lame coeff. μ_p (dyne/cm^2)	1.07×10^6
Length (cm)	6	Lame coeff . λ_p (dyne/cm^2)	4.28×10^6
wall thickness (cm)	0.1	k (cm^3 s/g)	5×10^{-9}
wall density (g/cm^3)	1.1	s_0 (cm^2/dyne)	5×10^{-6}
Fluid density (g/cm^3)	1	γ_f, γ_s	2500
Dynamic viscosity (poise)	0.035	Time step Δt	10^{-4} s
Biot-Willis constant, α	1	Final time	6 ms

In order to assess the impact of extending the study to finite elasticity we have performed two simulations, using hyperelastic model and linear elasticity model for the elastic skeleton of the porous media in the arterial wall. More precisely, in the latter we simplify the Green strain tensor to its linear part as $\boldsymbol{\varepsilon}(\boldsymbol{U}) = \frac{1}{2}(\nabla \boldsymbol{U} + \nabla \boldsymbol{U}^T)$ for the structure; and in the second simulation we use the complete Green strain tensor , $\boldsymbol{\varepsilon}(\boldsymbol{U}) = \frac{1}{2}(\nabla \boldsymbol{U} + \nabla \boldsymbol{U}^T + (\nabla \boldsymbol{U})\,\nabla \boldsymbol{U}^T)$. For each model (linear and nonlinear) we study the propagation of a single pressure wave following the pressure profile (31), with 2 different values for P_{max} ; one using reference value of P_{max} = 13334 dyne/cm^2 which generates small deformation in the structure called the "weak" wave, and the other one using $10\times P_{max}$, namely by increasing the pressure amplitude 10 times from its references value.

The inlet pressure pulse generates a wave that inflates the channel near the inlet, travels through the channel, and hits the outlet of the tube. We consider a point on the interface Γ, located halfway between the inlet and the outlet and plot the displacement of this point vs. time, depicted in Figure 2. When the applied pressure and the strains are small (left panel of Figure 2), the linear and nonlinear solutions nearly coincide and the displacement fields of the two cases almost match. However, when the strains become large (right panel), nonlinear effects become significant and we notice observable differences in the displacement magnitude. We observe that the displacements predicted by the small deformation model are consistently smaller than those predicted by the finite deformation model.

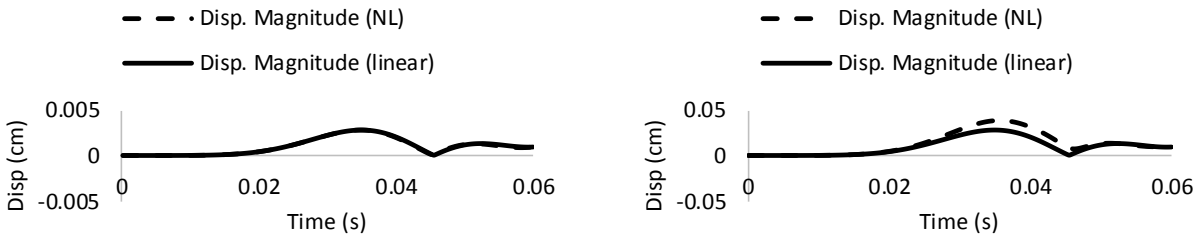

Figure 2. Left (weak pressure wave), right (strong pressure wave). The corresponding plots show a comparison for the displacement measured halfway between the inlet and the outlet for linear (dashed) and nonlinear (solid line) elasticity.

4.2 Benchmark Example 2 : FSI analysis of a cicular ring

In this example, we investigate the dynamical behavior of a poroelastic material which is subjected to a time dependent loading from the fluid. In particular, we focus on the quantitative analysis of energy balance and dissipation in FPSI models. We consider the problem of injecting an incompressible fluid in a poroelastic medium with a circular cross-section, which results in expansion of the structure. Flow in the porous media is driven by the injection into the fluid domain Ω_f. Then fluid is drained out of the media and poroelastic structure shrinks. In Figure 3 we illustrate a schematic representation of the fluid and structure regions.

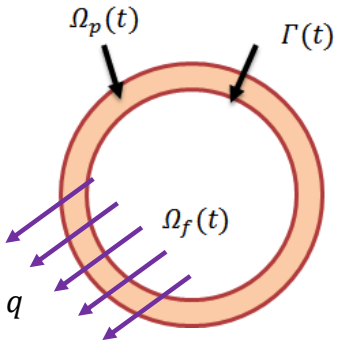

Figure 3. Schematic of the geometrical model for benchmark problem 2.

We consider nonlinear, poroelastic, isotropic, and nearly incompressible ring with the inner radius R_i and outer radius equal to R_o. Its dimensions are provided in Table 2. A source term g is considered in the mass balance equation to model the injection, namely

$$\nabla \cdot \boldsymbol{v} = g \qquad in\ \Omega_f(t)$$

All simulations in this part have been performed using a sine-type source

$$g(t) = g_{max}\left(\sin\left(\frac{\pi t}{T_{max}}\right)\right) \quad if \ \ t \le T_{max} \tag{32}$$

The injection parameters are chosen such that we enforce a reasonable volumetric flow rate Q, sufficient to inflate the poroelastic wall up to the large deformation regime and is calculated based on $g(t) = \frac{Q(t)}{Area(t)}$. For this simulation, zero pore pressure on the outer boundary is included in our model.

Table 2. Physical and numerical parameters for benchmark problem 2

Parameters	values	Parameters	values
R_i (cm)	0.5	Lame coeff. μ_p (dyne/cm^2)	1.07×10^6
R_o (cm)	0.4	Lame coeff . λ_p (dyne/cm^2)	4.28×10^6
wall thickness (cm)	0.1	k (cm^3 s/g)	5×10^{-9}
wall density (g/cm^3)	1.1	s_0 (cm^2/dyne)	5×10^{-6}
Fluid density (g/cm^3)	1	γ_f, γ_s	2500
Dynamic viscosity (poise)	0.035	Time step Δt	10^{-4} s
Biot-Willis constant, α	1	Final time	6 ms

Plots in Figure 4 show the filtration velocity and the pressure through the thickness of the wall, due to steadily increasing internal pressure obtained using $g_{max} = 30\ s^{-1}$ and $T_{max} = 0.003\ s$. Since fluid pressure is constrained to be zero at the outer radial surface, Darcy pressure starts from zero at the exterior surface and reaches its maximum at the inner surface. We observe that since we use mixed formulation for the Darcy's equation, the model accurately captures the variations in fluid pressure and flow velocity across the thickness. We also notice that in Figure 4 the magnitude of outgoing flow on the outer surface is almost zero (less than 0.02 cm/s). Therefore, although we did not impose the no-flow boundary condition on the outer surface, it has been satisfied simultaneously to the zero pressure condition. The reason is that in this benchmark problem, the loading changes occur quickly and propagate slowly in the relatively low permeability environment, from the interior to the exterior of the circular domain. As a result, it seems that the outer boundary condition doesn't play a role in our case.

A remarkable feature of the numerical results is that the velocity field in the porous matrix has a large variation in the radial direction. Indeed, in Figure 4 we observe that the filtration velocity changes through the wall thickness and so $\nabla \cdot \boldsymbol{q} \neq 0$. For an incompressible flow in a rigid porous matrix that behavior would violate the divergence free constraint, arising from the mass conservation principle. However, in a poroelastic material this effect is possible, because the velocity in the porous matrix obeys to the equation $(\frac{D}{Dt}\left(s_0 p_p + \nabla . \boldsymbol{U}\right) + \nabla \cdot \boldsymbol{q} = 0)$. More

precisely, Figure 5 shows the time variation of the different components of this expression for benchmark problem 2. We observe that, although $\nabla \cdot \boldsymbol{q}$ is large, the residual of this equation is almost zero, which confirms that mass balance is satisfied in the porous matrix.

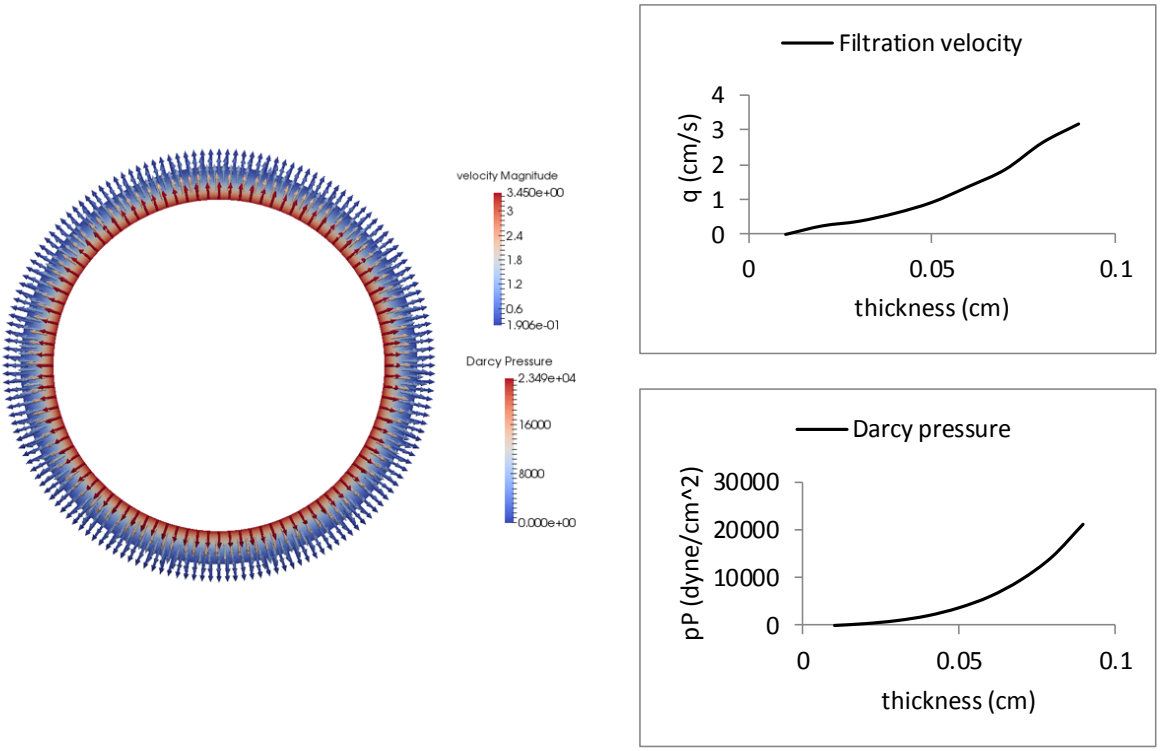

Figure 4. Filtration velocity (the arrows denote the orientation not the magnitude) and Darcy pressure through the wall thickness at t=2ms for the test case with loading period=6ms and $k=5\times10^{-6}$ cm^3 s/g One dimensional plots are obtained along the left hand side intersection of the ring with the *x* axis.

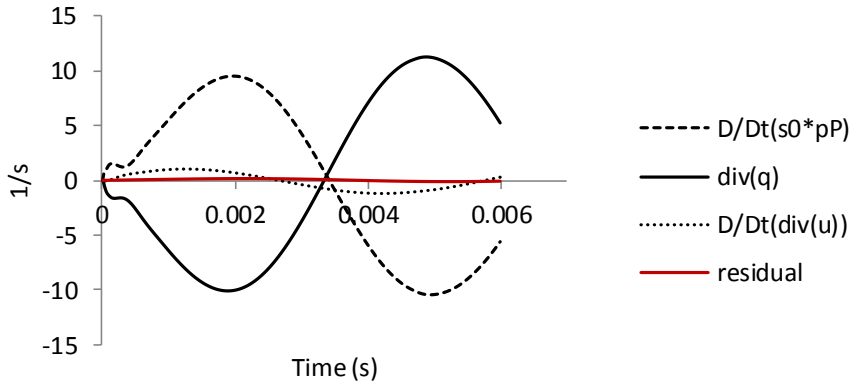

Figure 5. Time variation of mass conservation terms in the Biot model through the wall thickness

To determine the adequate mesh size to use, a mesh sensitivity analysis has been carried out on our 2D cross sectional model. We solved several test cases with different mesh sizes of the structure using the reference parameters provided in Table 2.

Table 3. Mesh sensitivity results

	# of cell in Ω_p	$P_f \times 10^4$ (dyne/cm^2)	Time step size	$P_f \times 10^4$ (dyne/cm^2)
Mesh 1	1788	2.40	Δt	2.48
Mesh 2	3992	2.48	$\Delta t/2$	2.49
Mesh 3	9194	2.51		

We have compared the difference in the fluid pressure-wall displacement loop between the three different mesh sizes presented in the left panel of Figure 6. To this purpose, we define a quantitative indicator as the pressure in the loading curve observed at 0.01 cm of displacement (right panel of Figure 6). The results are provided in Table 3 and Figure 7. The mesh sensitivity analysis shows that for computational meshes equal of finer than Mesh 2, results are almost insensitive to increasing the number of nodes. Therefore, Mesh 2 has been used for all the following tests in the sensitivity analysis. Moreover, to study the convergence in time, we compare the solution using different time steps using the same indicator we have used for the mesh convergence. Results confirm that our reference time step $\Delta t=1\times10^{-5}$s provides satisfactory approximation.

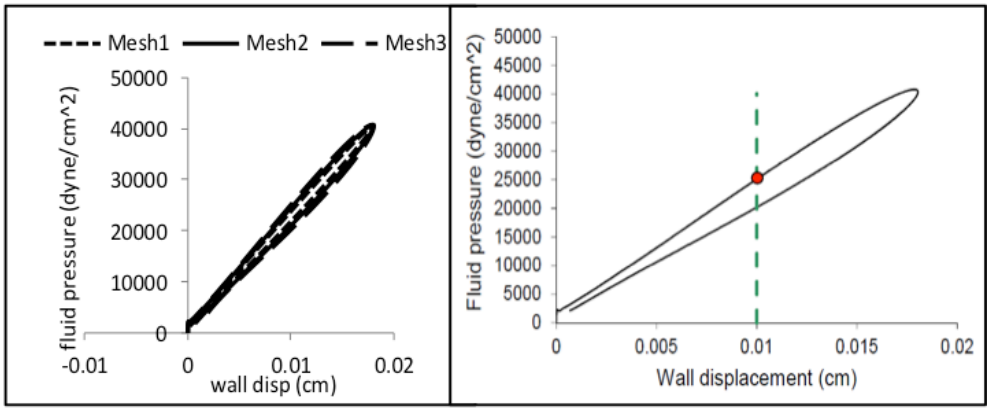

Figure 6 Hysteresis loop for different mesh size (left), Schematic description of the quantitative indicator used in the sensitivity analysis (right)

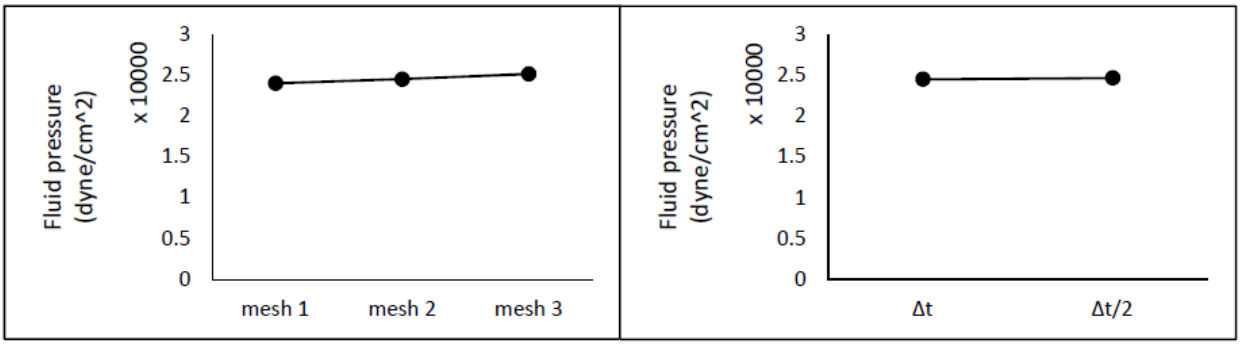

Figure 7. Sensitivity analysis plots for different mesh sizes (left) and time steps (right)

4.3 Sensitivity analysis of the model parameters

To show the importance of using a poroelastic model for soft biological tissue, we investigate the effects of the material properties of the poroelastic model on the fluid pressure vs the structure deformation loop. Our objective is exploring in what condition the poroelastic model is dissipative. More precisely we want to examine the range of model parameters that generate a pressure relaxation loop, i.e. a cyclic loading loop where the pressure in the loading phase is higher than the one in the corresponding unloading part of the cycle, see Figure 6 (right panel) for a schematic illustration. With a little abuse of notation, this effect is called *hysteresis loop* from now on. We show that different values of the storativity coefficient and hydraulic conductivity lead to differences in the hysteresis loop. We also look at the dependence of the hysteresis loop on the stiffness of the poroelastic matrix and the loading rate.

4.3.1 Effect of hydraulic conductivity (k)

Figure 8 informs us about the sensitivity of the hysteresis loop with respect to the hydraulic conductivity. We compare the results obtained using three exponentially increasing values of the hydraulic conductivity k=5×10^{-9},5×10^{-8},5×10^{-6} cm^3 s/g, starting from the reference values of

Table 2. We observe that increasing the hydraulic conductivity, increases the area of the hysteresis loop.

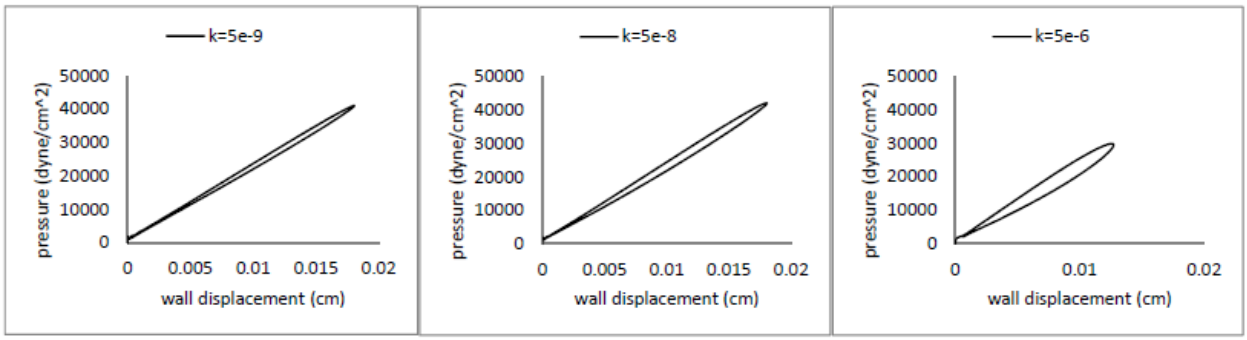

Figure 8. Comparing hysteresis loops for different values of hydraulic conductivity *k*

4.3.2 Effect of loading period (T_{max}) and source term amplitude (g_{max})

We consider three different amplitude of the sine-type source term. We change amplitude such that we inject the same amount of fluid at different loading periods, see Figure 9 for an illustration.

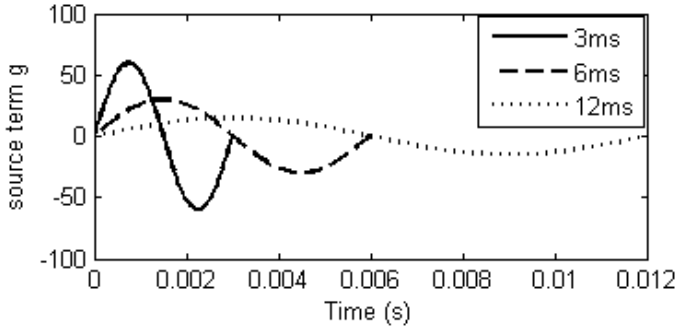

Figure 9. Different values of source term *g,* used to obtain the results of Figure 10a.

As a result, T_{max} assumes the values of 3ms, 6ms, 12ms. We define loading rate as the inverse of loading period, namely $\frac{1}{T_{max}}$. In Figure 10(a),(b), the hysteresis loop for different loading rates and different amplitudes of the source term are analyzed. The hydraulic conductivity has been set to the value of k=5×10^{-6} cm^2.s/g. We observe that the fluid pressure dissipates more in the high loading rate regime. Furthermore, by increasing amplitude of g the area of the hysteresis loop increases significantly. Figure 10(c) shows the comparison of the fluid and Darcy pressure as well as the displacement and filtration velocity vectors obtained in different loading rate regimes. In the case of high loading rate (3ms loading period), plots in Figure 10(c) show that the time variation of Darcy pressure, namely *dPp/dt*, is bigger and there exists a large pore pressure gradient (*dPp/dx*) from the beginning of the simulation. Hence, the filtration velocity can attain high values more quickly; as thus the energy loss occurs much faster than for the small loading rate (12ms loading period) due to the rapid fluid flow.

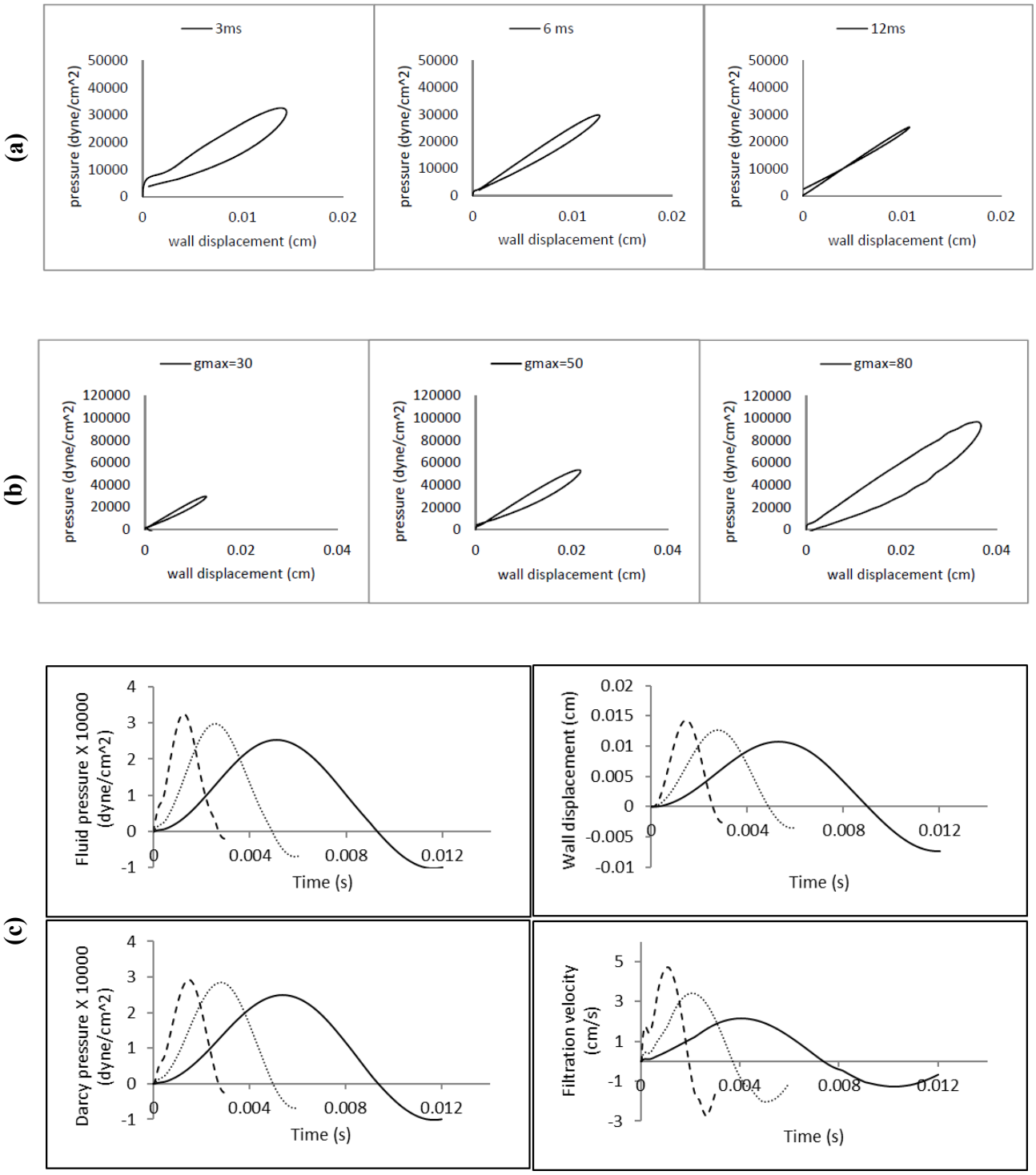

Figure 10. Comparing hysteresis loops for different values of loading period, with $k=5\times10^{-6}$ cm^3 s/g (a), Comparing hysteresis loops for different values of the source term *g*, loading period=6ms (b), Comparing fluid pressure, wall displacement, Darcy pressure and filtration velocity for different values of loading period, 3ms (dashed), 6ms (dotted), and 12ms (solid) lines (c)

4.3.3 **Effect of storage coefficient (s_0)**

To complete the description of the mechanical response of the tissue under fluid infiltration, we analyze how the storage of the fluid within the material changes due to the stress and pressurization. Under the assumption of full saturation of all the connected pore space, this corresponds to vary the storativity coefficient. We remind that the storage coefficient modulates the decrease of the material porosity with respect to the increasing pore pressure. In other words, it is related to the compressibility of the poroelastic system. From Figure 11 we see that changing this coefficient from the reference value presented in Table 2, causes a significant difference in the hysteresis loop. In other words, increasing s_0 leads to increase of the fluid content in the porous medium, which results in more dissipation.

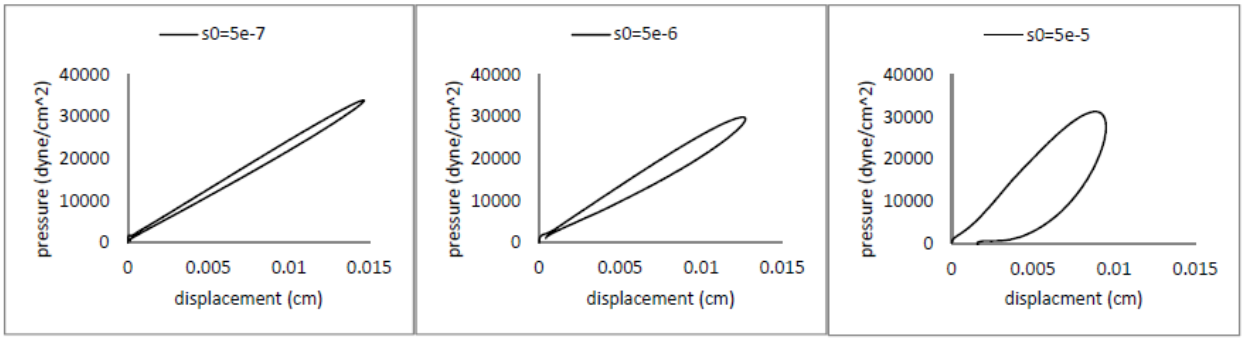

Figure 11. Comparing hysteresis loops for different values of storage coefficient s_0

4.3.4 **Effect of Young's modulus (E)**

We investigate the influence of Young's modulus E on the hysteresis loop. We use k=5×10^{-6} cm^2.s/g and the loading period of 6ms for these simulations. We study the behavior of the system when we vary the Young modulus 10 times from its reference value. In Figure 12(a), we show the effect of changing Young modulus of the elastic skeleton on energy dissipation. For the same simulations, pressure values in the fluid and porous media as well as velocity and displacement fields are shown in Figure 12(b). Results clearly show that very stiff materials behave as if a single-phase elastic model were used.

5 Discussion

We study the energy dissipation in a poroelastic material, determined by numerically solving Biot's equations of poroelasticity for the interaction between the fluid and a poroelastic structure. Dissipation in porous media is the result of the relative motion between the pore fluid flow and the skeleton [33] defined as the filtration velocity ($\boldsymbol{q}$) in this work. According to [49] and [50] viscous forces retard the filtration velocity within the structure and the relative fluid movement causes energy loss. We have analyzed the influence of the model parameters on these effects. Our results suggest that energy loss depends both on the fluid filtration speed ($\boldsymbol{q}$) and on the

poroelastic parameters (hydraulic conductivity k and storativity s_0). The magnitude of displacement has a significant effect on the energy dissipation in the poroelastic model and the dynamic behavior amplifies the energy loss. In other words, when the model is subject to high internal pressure gradients, which are producing large filtration fluid flow such as in benchmark 2, then poroelastic material behavior and energy dissipation are noticeable. For the benchmark 1, the volumetric deformation rate is small and filtration velocity is negligible. Hence, the poroelastic model features time-dependent behavior associated primarily with the solid-phase deformation and the effect of poroelasticity on hysteresis loop is negligible.

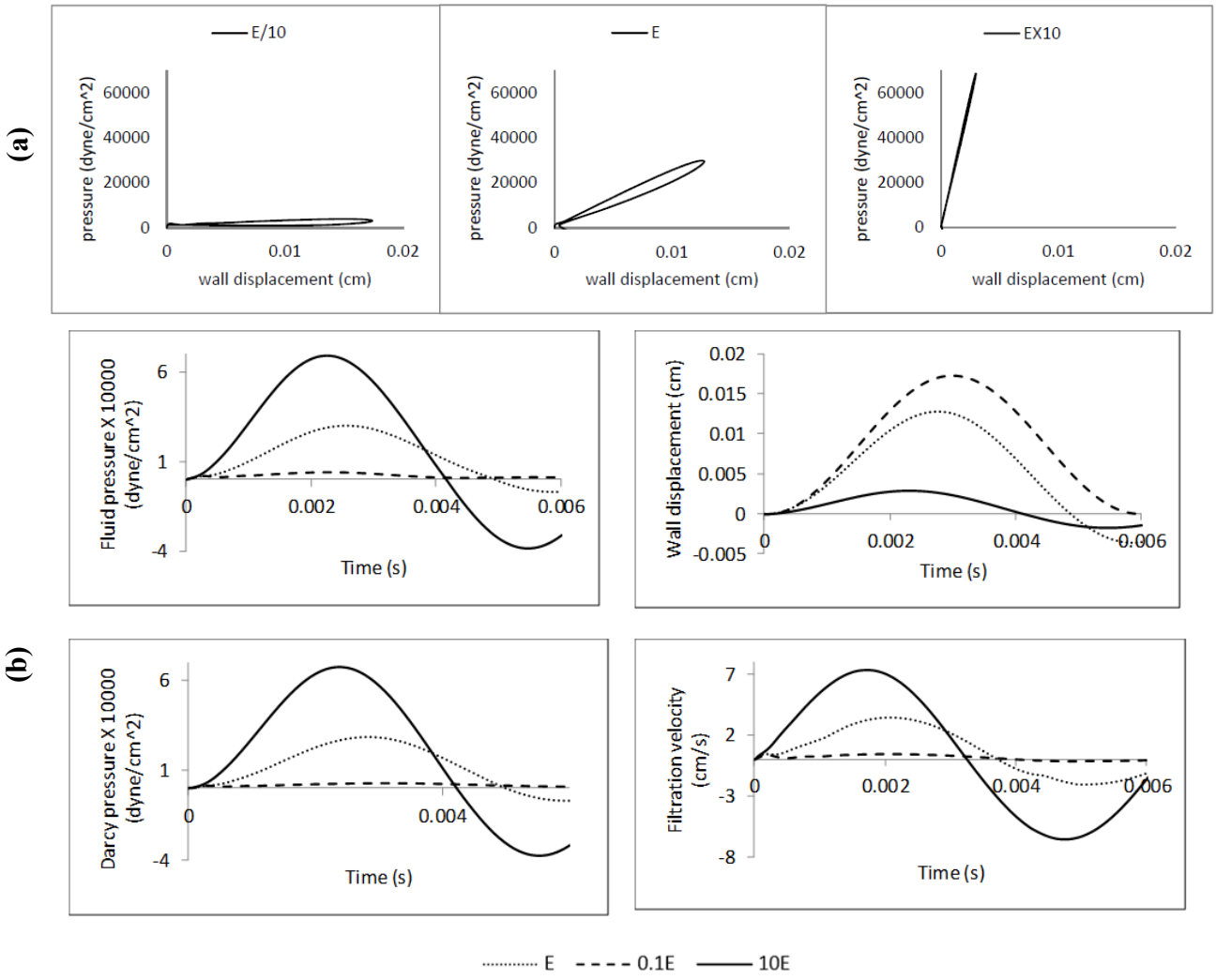

Figure 12. Comparing hysteresis loop for different values of Young's modulus (a) . Comparing fluid pressure, wall displacement, Darcy pressure and filtration velocity for different values of Young's modulus,$\mathbf{0.1}\times\boldsymbol{E}$ (dashed), $\boldsymbol{E}$ (dotted), and $\mathbf{10}\times\boldsymbol{E}$ (solid) lines (b)

When the load frequency is low, the fluid flows slowly through the porous medium, so that little energy is lost due to the viscosity of the fluid filling the pores in a periodic loading cycle. Therefore, the behavior of the system approaches that of an elastic system. The same is true for very small hydraulic conductivity values. In the opposite situation, if load is applied abruptly to a poroelastic material, the energy dissipation is significant since the flow through the wall increases, as confirmed by the results in Figure 10. This observation is in agreement with results obtained in [51] for the dynamic stability of the poroelastic medium. The idea of dependency of the energy dissipation to the load frequency is also investigated in [52]. There, the authors evaluated the complex dynamic modulus of the poroelastic media, which is a measure of damping in the system. They show that there is a frequency at which maximum loss modulus occurs and it depends on the dissipation coefficient and the length to thickness ratio of the poroelastic slab. By comparing the time-dependent deformation properties of the poroelastic medium framework with a viscoelastic model, one can identify the similarities of poroelasticity and viscoelasticity. In [6] it is stated that a porous model has the viscoelastic character typical of a soft biological tissue, because of the motion of the fluid in the pores. Poroelasticity and viscoelasticity may result in the similar energy dissipation in experiments, and this work gives a mechanistic explanation of this analogy.

Finally, we define and analyze a *quantitative indicator* of the hysteresis cycle amplitude that we call for simplicity the *hysteresis amplitude* (HA). It measures the amplitude of the cycle as the difference of pressure in the loading and unloading curves at 75% of maximum displacement (Figure 13). In all charts, this indicator ranges between 2000 and 30000 dyne/cm^2. Using the numerical experiments of Figure 8-Figure 12, we have studied the variation of HA when each parameter, namely storativity, hydraulic conductivity, loading frequency and young modulus, is varied individually. The outcome of the analysis is reported in Figure 14.

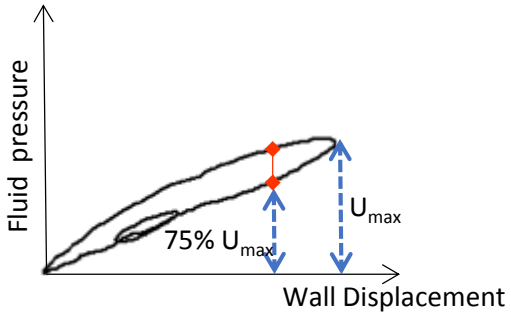

Figure 13. Schematic of the measuring indicator used in the sensitivity analysis

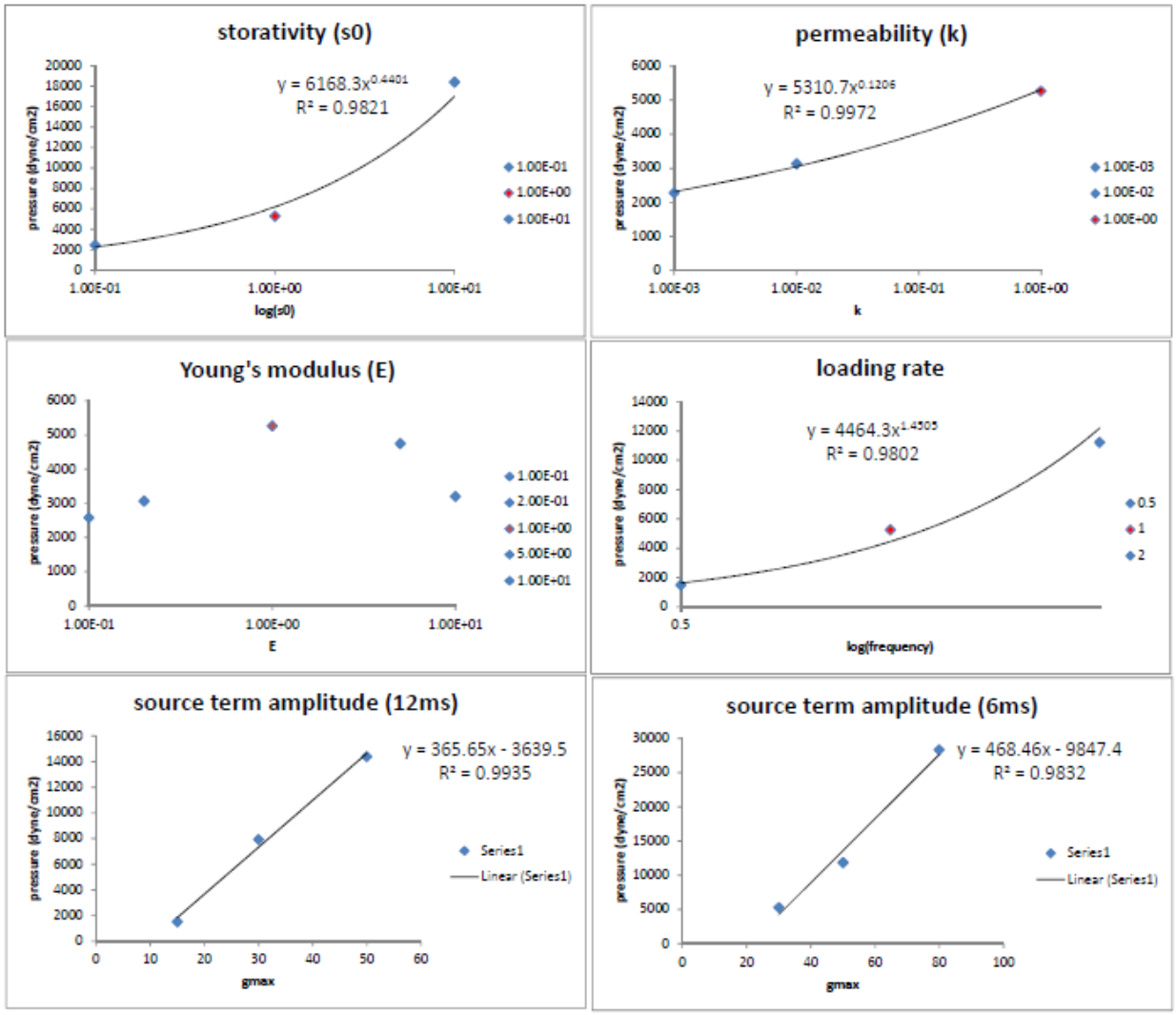

Figure 14. Sensitivity results for dependence of hysteresis loop to the model parameters

For a better comparison of the different charts, the parameters are normalized with respect to a reference values that are chosen as follows: s_0=5×10^{-6} cm^2/dyne, k=5×10^{-6} cm^2.s/g, loading rate = 1/0.006, E=1×10^7. The data points corresponding to the reference value are highlighted in red. We observe that the amplitude of the hysteresis cycle increases with increasing the storativity, hydraulic conductivity and loading rate. We also observe that the dependence of the hysteresis amplitude from the parameters is nonlinear. Since the data for storativity, hydraulic conductivity and loading frequency feature a similar increasing trend, we have fitted them using a power law model, namely $y = c.x^p$, where (p) is the exponent that quantifies the sensitivity of the quantity of interest (y) with respect to the control parameter (x) and c is a scaling constant. We observe that, thanks to the renormalization, all the charts show a similar behavior and the scaling constants are comparable, but the exponents of the power law are different. In particular, the

loading frequency features the maximum impact on the hysteresis, followed by the storativity and the hydraulic conductivity (Table 4). The dependence of hysteresis cycle to the Young modulus has a different interpretation. Increasing Young modulus leads to decrease in wall displacement and increase in filtration velocity at the same time (Figure 12, b). We believe our analysis substantially show that the area inside the pressure-displacement cycle is barely affected by the stiffness of the material, however, based on the results of Figure 14, there is an optimum value for Young modulus such that maximum HA occurs. The last row of the plots in Figure 14 shows the variation of the pressure-displacement cycle when we vary the amplitude of the source term. This analysis is performed for two different loading rates. In both cases, we observe a linear dependence of the hysteresis amplitude from the source term magnitude.

Table 4. Exponent of the power law for different parameters of the sensitivity analysis

Parameter	value of the exponent (p) in $y = c.x^p$
Loading rate	1.4505
Storativity	0.4401
Hydraulic conductivity	0.1206

6 Conclusions

We have developed a framework for the numerical simulations of Fluid-Porous Structure Interaction (FPSI) problems using the finite element method. Results of this study show that the mechanism of the energy dissipation of a poroelastic material is different from that of a conventional solid material, because of the interaction between the fluid and solid phases. More precisely, according to the model for poroelasticity adopted here, the energy dissipation takes place because the skeleton is permeated with fluid and also the magnitude of energy dissipation varies significantly with the parameters of the poroelastic model. These results should however be more thoroughly validated, in particular with respect to the assumptions at the basis of the model, such as the application of Athy's model to the case of soft tissues. Future developments of this study will focus on applying the model to more complicated geometries, in order to reach the goal of simulating realistic vascular districts. Another extension of this work will be to simulate mass transport or drug delivery through the arterial walls, coupled with the pulsatile blood flow.

Acknowledgements

This work has been supported by the fellowship from Computational Modeling & Simulation PhD program, University of Pittsburgh.

Conflict of Interest

The authors declare that they have no conflict of interest.

References

1. Chapelle, D., et al., *A poroelastic model valid in large strains with applications to perfusion in cardiac modeling.* Computational Mechanics, 2009. **46**(1): p. 91-101.
2. Chabiniok, R., et al., *Multiphysics and multiscale modelling, data–model fusion and integration of organ physiology in the clinic: Ventricular cardiac mechanics.* Interface Focus, 2016. **6**(2).
3. Calo, V.M., et al., *Multiphysics model for blood flow and drug transport with application to patient-specific coronary artery flow.* Computational Mechanics, 2008. **43**(1): p. 161-177.
4. Feenstra, P.H., et al., *Drug transport in artery walls: A sequential porohyperelastic-transport approach.* Computer Methods in Biomechanics and Biomedical Engineering, 2009. **12**(3): p. 263-276.
5. Badia, S., et al., *Coupling Biot and Navier-Stokes equations for modelling fluid-poroelastic media interaction.* Journal of Computational Physics, 2009. **228**(21): p. 7986-8014.
6. Koshiba, N., et al., *Multiphysics simulation of blood flow and LDL transport in a porohyperelastic arterial wall model.* J Biomech Eng, 2007. **129**(3): p. 374-85.
7. McCutchen, C.W., *Cartilage is poroelastic, not viscoelastic (including and exact theorem about strain energy and viscous loss, and an order of magnitude relation for equilibration time).* Journal of Biomechanics, 1982. **15**(4): p. 325-327.
8. Yang, Z., et al., *Dynamic finite element modeling of poroviscoelastic soft tissue.* Computer Methods in Biomechanics and Biomedical Engineering, 2006. **9**(1): p. 7-16.
9. Armstrong, M.H., et al., *A finite element model for mixed porohyperelasticity with transport, swelling, and growth.* PLoS ONE, 2016. **11**(4).
10. Goriely, A., et al., *Mechanics of the brain: perspectives, challenges, and opportunities.* Biomechanics and Modeling in Mechanobiology, 2015. **14**(5): p. 931-965.
11. Bukac, M., et al., *Effects of Poroelasticity on Fluid-Structure Interaction in Arteries: a Computational Sensitivity Study*, in *Modeling the Heart and the Circulatory System*. 2015, Springer. p. 197-220.
12. Bazilevs, Y., et al., *Isogeometric fluid-structure interaction analysis with applications to arterial blood flow.* Computational Mechanics, 2006. **38**(4-5): p. 310-322.
13. Bazilevs, Y., et al., *Patient-specific isogeometric fluid–structure interaction analysis of thoracic aortic blood flow due to implantation of the Jarvik 2000 left ventricular assist device.* Computer Methods in Applied Mechanics and Engineering, 2009. **198**(45–46): p. 3534-3550.
14. Crosetto, P., et al., *Fluid–structure interaction simulation of aortic blood flow.* Computers & Fluids, 2011. **43**(1): p. 46-57.
15. Chepelenko, G.V., *Atherosclerosis regulation via media lipid-driven VSMC cholesterol efflux switch.* Medical Hypotheses, 2015. **84**(2): p. 141-144.
16. Smith, E., *Transport, interactions and retention of plasma proteins in the intima: the barrier function of the internal elastic lamina.* European heart journal, 1990. **11**(suppl E): p. 72-81.
17. Zakerzadeh, R., et al., *Computational analysis of energy distribution of coupled blood flow and arterial deformation.* International Journal of Advances in Engineering Sciences and Applied Mathematics, 2015: p. 1-16.

18. Burtschell, B., et al., *Effective and energy-preserving time discretization for a general nonlinear poromechanical formulation.* Computers & Structures, 2017. **182**: p. 313-324.
19. Vuong, A.T., et al., *A general approach for modeling interacting flow through porous media under finite deformations.* Computer Methods in Applied Mechanics and Engineering, 2015. **283**: p. 1240-1259.
20. Chapelle, D., et al., *General coupling of porous flows and hyperelastic formulations—From thermodynamics principles to energy balance and compatible time schemes.* European Journal of Mechanics - B/Fluids, 2014. **46**: p. 82-96.
21. Balzani, D., et al., *Numerical modeling of fluid–structure interaction in arteries with anisotropic polyconvex hyperelastic and anisotropic viscoelastic material models at finite strains.* International journal for numerical methods in biomedical engineering, 2015.
22. Tricerri, P., et al., *Fluid-structure interaction simulations of cerebral arteries modeled by isotropic and anisotropic constitutive laws.* Computational Mechanics, 2015. **55**(3): p. 479-498.
23. Bukač, M., et al., *Partitioning strategies for the interaction of a fluid with a poroelastic material based on a Nitsche's coupling approach.* Computer Methods in Applied Mechanics and Engineering, 2015. **292**: p. 138-170.
24. Zakerzadeh, R., et al., *Fluid-Structure Interaction in Arteries with a Poroelastic Wall Model.* 21st Iranian Conference of Biomedical Engineering (ICBME) IEEE,: p. 35 - 39.
25. Dunne, T., et al., *Numerical simulation of fluid-structure interaction based on monolithic variational formulations.* Fundamental trends in fluid–structure interaction, Contemp. Chall. Math. Fluid Dyn. Appl, 2010. **1**: p. 1-75.
26. Burman, E., et al., *Explicit strategies for incompressible fluid-structure interaction problems: Nitsche type mortaring versus Robin–Robin coupling.* International Journal for Numerical Methods in Engineering, 2014. **97**(10): p. 739-758.
27. Hansbo, P., *Nitsche's method for interface problems in computa-tional mechanics.* GAMM-Mitteilungen, 2005. **28**(2): p. 183-206.
28. Yang, M., et al., *The possible role of poroelasticity in the apparent viscoelastic behavior of passive cardiac muscle.* J Biomech, 1991. **24**(7): p. 587-97.
29. Taber, L.A., et al., *Poroelastic plate and shell theories*, in *Mechanics of Poroelastic Media*. 1996, Springer. p. 323-337.
30. Biot, M.A., *General theory of three-dimensional consolidation.* Journal of Applied Physics, 1941. **12**(2): p. 155-164.
31. Biot, M.A., *Theory of elasticity and consolidation for a porous anisotropic solid.* Journal of Applied Physics, 1955. **26**(2): p. 182-185.
32. Biot, M.A., *General solutions of the equations of elasticity and consolidation for a porous material.* J. Appl. Mech., 1956. **23**(1): p. 91-96.
33. Biot, M.A., *Theory of propagation of elastic waves in a fluid‐saturated porous solid. I. Low‐frequency range.* The Journal of the acoustical Society of america, 1956. **28**(2): p. 168-178.
34. Discacciati, M., et al., *Navier-Stokes/Darcy coupling: modeling, analysis, and numerical approximation.* Revista Matemática Complutense, 2009. **22**(2): p. 315-426.
35. Quaini, A., et al., *A semi-implicit approach for fluid-structure interaction based on an algebraic fractional step method.* Mathematical Models and Methods in Applied Sciences, 2007. **17**(6): p. 957-983.
36. Uzuoka, R., et al., *Dynamics of unsaturated poroelastic solids at finite strain.* International Journal for Numerical and Analytical Methods in Geomechanics, 2012. **36**(13): p. 1535-1573.
37. Coussy, O., *Poromechanics*. 2004: Wiley.
38. Girault, V., et al., *A lubrication fracture model in a poro-elastic medium.* Mathematical Models and Methods in Applied Sciences, 2015. **25**(4): p. 587-645.

39. Fowler, A.C., et al., *Fast and slow compaction in sedimentary basins.* SIAM Journal on Applied Mathematics, 1998. **59**(1): p. 365-385.
40. Holzapfel, G.A., *Nonlinear solid mechanics: a continuum approach for engineering science.* Meccanica, 2002. **37**(4): p. 489-490.
41. Burman, E., et al., *Stabilization of explicit coupling in fluid-structure interaction involving fluid incompressibility.* Computer Methods in Applied Mechanics and Engineering, 2009. **198**(5-8): p. 766-784.
42. Quarteroni, A., et al., *Numerical mathematics*. Vol. 37. 2010: Springer Science & Business Media.
43. Razzaq, M., et al., *Numerical Simulation and Benchmarking of Fluid Structure Interaction with Application to Hemodynamics*. 2009: Techn. Univ., Fak. für Mathematik.
44. Jendoubi, A., et al., *A simple mesh-update procedure for fluid–structure interaction problems.* Computers & Structures, 2016. **169**: p. 13-23.
45. Hecht, F., *New development in freefem+.* Journal of Numerical Mathematics, 2012. **20**(3-4): p. 251-265.
46. Brooks, A.N., et al., *Streamline upwind/Petrov-Galerkin formulations for convection dominated flows with particular emphasis on the incompressible Navier-Stokes equations.* Computer methods in applied mechanics and engineering, 1982. **32**(1): p. 199-259.
47. Ijiri, T., et al., *A Kinematic Approach for Efficient and Robust Simulation of the Cardiac Beating Motion.* PLoS ONE, 2012. **7**(5): p. e36706.
48. Bukač, M., et al., *Fluid-structure interaction in blood flow capturing non-zero longitudinal structure displacement.* Journal of Computational Physics, 2013. **235**: p. 515-541.
49. Ren, H., et al., *Poroelastic analysis of permeability effects in thinly layered porous media.* Geophysics, 2009. **74**(6): p. N49-N54.
50. Costi, J.J., et al., *Frequency-dependent behavior of the intervertebral disc in response to each of six degree of freedom dynamic loading: solid phase and fluid phase contributions.* Spine, 2008. **33**(16): p. 1731.
51. Cederbaum, G., et al., *Poroelastic structures*. 2000: Elsevier.
52. Yeh, F.-H., et al., *Dynamic behavior of a poroelastic slab subjected to uniformly distributed impulsive loading.* Computers & Structures, 1998. **67**(4): p. 267-277.

MOX Technical Reports, last issues

Dipartimento di Matematica
Politecnico di Milano, Via Bonardi 9 - 20133 Milano (Italy)

60/2018 Zakerzadeh, R.; Zunino P.
A Computational Framework for Fluid-Porous Structure Interaction with Large Structural Deformation

59/2018 Martino, A.; Guatteri, G.; Paganoni, A. M.
Multivariate Hidden Markov Models for disease progression

56/2018 Antonietti, P.F.; Manzini, G.; Verani, M.
The conforming virtual element method for polyharmonic problems

57/2018 Ferro, N.; Micheletti, S.; Perotto, S.
POD-assisted strategies for structural topology optimization

58/2018 Ferro, N.; Micheletti, S.; Perotto, S.
A sequential coupling of shape and topology optimization for structural design

55/2018 Cerroni, D.; Laurino, F.; Zunino, P.
Mathematical analysis, finite element approximation and numerical solvers for the interaction of 3D reservoirs with 1D wells

54/2018 Dal Santo, N.; Deparis, S.; Manzoni, A.; Quarteroni, A.
Multi space reduced basis preconditioners for parametrized Stokes equations

53/2018 Giantesio, G.; Musesti, A.; Riccobelli, D.
A comparison between active strain and active stress in transversely isotropic hyperelastic materials

52/2018 Possenti, L.; di Gregorio, S.; Gerosa, F.M.; Raimondi, G.; Casagrande, G.; Costantino, M.L.; Z
A computational model for microcirculation including Fahraeus-Lindqvist effect, plasma skimming and fluid exchange with the tissue interstitium

51/2018 Stella, S.; Vergara, C.; Giovannacci, L.; Quarteroni, A.; Prouse, G.
Assessing the disturbed flow and the transition to turbulence in the arteriovenous fistula